Journal of Structural Geology 96 (2017) 134–148

Contents lists available at ScienceDirect

Journal of Structural Geology

journal homepage: www.elsevier.com/locate/jsg

Fracture network, fluid pathways and paleostress at the Tolhuaca geothermal field

Pamela Pérez-Flores [a, b, *], Eugenio Veloso [a, b], José Cembrano [a, b], Pablo Sánchez-Alfaro [b, c], Martín Lizama [b, c], Gloria Arancibia [a, b]

[a] Departamento de Ingeniería Estructural y Geotécnica, Pontificia Universidad Católica de Chile, Avenida Vicuña Mackenna 4860, Macul, Santiago, Chile
[b] Andean Geothermal Center of Excellence (CEGA, FONDAP-CONICYT), Santiago, Chile
[c] Departamento de Geología, Universidad de Chile, Santiago, Chile

ARTICLE INFO

Article history:
Received 4 October 2016
Received in revised form
23 January 2017
Accepted 25 January 2017
Available online 30 January 2017

Keywords:
Tolhuaca geothermal field
Paleomagnetic core reorientation
Stress field
Liquiñe-Ofqui fault system

ABSTRACT

In this study, we examine the fracture network of the Tolhuaca geothermal system located in the Southern Andean volcanic zone that may have acted as a pathway for migration and ascent of deep-seated fluids under the far/local stress field conditions of the area. We collected the orientation, slip-data and mineralogical content of faults and veins recovered on a ca. 1000 m deep borehole (Tol-1) located in the NW-flank of the Tolhuaca volcano. Tol-1 is a non-oriented, vertical borehole that recovered relatively young (<1 Ma) basaltic/andesitic volcanic rocks with subordinate pyroclastic/volcanoclastic interbedded units of Pleistocene age. Here, we examined and measured the inclination, geometry, texture, mineralogy, and relative sense of displacement of veins and faults. To determine the actual azimuthal orientation of fault and veins we reoriented 66 segments (89 standard mini-cores) of Tol-1 using stable Characteristic remanent magnetization component (ChRM) obtained by thermal demagnetization methodology. Paleo-declination of ChRM vectors was used to re-orient the borehole pieces, as well as fault and veins, to a common anchor orientation value consistent with the Geocentric Axial Dipole approximation (GAD). Inversion of RM-corrected fault-slip data reveals a local tensional stress field with a vertically oriented σ_1 axis (083/74) and a subhorizontal, NS-trending σ_3 axis (184/03). Within the topmost 400 m of the borehole, faults and veins are randomly oriented, whereas below 400 m depth, faults and veins show preferential NE-to EW-strikes and steep (>50°) dips. The EW-striking veins are compatible with the calculated local stress field whereas NE-striking veins are compatible with the regional stress field, the morphological elongation of volcanic centers, alignments of flank vents and dikes orientation. Our results demonstrate that the paleomagnetic methodology proved to be reliable and it is useful to re-orient vertical boreholes such as Tol-1. Furthermore, our data show that the bulk transpressional regional stress field has local variations to a tensional stress field within the NE-striking fault zone belonging to the Liquiñe-Ofqui Fault System, favoring the activation of both NW- and NE-striking pre-existent discontinuities, especially the latter which are favorably oriented to open under the prevailing stress field. The vertical σ_1 and NS-trending subhorizontal σ_3 calculated in the TGS promote the activation of EW-striking extensional veins and both NE and NW-striking hybrid faults, constituting a complex fluid pathway geometry of at least one kilometer depth.

1. Introduction

Tectonic activity in areas of intense heat flux, controls the dynamics of deformation, fluid-flow ascent and heat transfer (e.g. Barnhoorn et al., 2010; Nakamura, 1977; Sibson, 1996). These processes lead to the generation of structural elements (fault, veins, and joints), which are arranged as a complex fracture network. These structural elements are important pathways for the

* Corresponding author. Departamento de Ingeniería Estructural y Geotécnica, Pontificia Universidad Católica de Chile, Avenida Vicuña Mackenna 4860, Macul, Santiago, Chile.
E-mail addresses: pvperez1@uc.cl (P. Pérez-Flores), anveloso@ing.puc.cl (E. Veloso), jcembrano@ing.puc.cl (J. Cembrano), vsanchez@ing.uchile.cl (P. Sánchez-Alfaro), mc.lizama@gmail.com (M. Lizama), garancibia@ing.puc.cl (G. Arancibia).

http://dx.doi.org/10.1016/j.jsg.2017.01.009
0191-8141/

migration, ascent and/or emplacement of deep-seated fluids in hydrothermal systems because primary permeability and porosity is continuously sealed by hydrothermal mineralization (e.g. Bons et al., 2012; Rowland and Sibson, 2004; Zhang et al., 2008). Examining the nature, spatial distribution, and geometry of such fracture network can help to unravel the fundamental geological processes operating on both ancient and active geothermal systems (e.g. Brogi, 2008; Curewitz and Karson, 1997; Rowland et al., 2012).

Surface structural mapping of fault-fracture networks in active geothermal systems helps understanding the overall geometry and preferential orientation of fluid pathways– and eventually the nature of heat transfer – yet these are only proxies of the actual conditions operating at depth (Nukman and Moeck, 2013). Subsurface information can be collected using geophysical methods or by means of coring and drilling. Structural elements contained on recovered whole rock drilling pieces can then be spatially oriented with respect to the core axis, providing valuable inclination-only data about the general and downhole distribution of geological elements (e.g. Dobson et al., 2003; Ganerød et al., 2008; Moncada et al., 2012). However, random rotations of the rock pieces about the axis of the core prevent direct measurements of azimuthal data. Then, it becomes necessary to re-orient recovered rock pieces into the geographic coordinate system, to further re-orient measured structural elements. Re-orientation techniques are varied (e.g. MacLeod et al., 1994; Ureel et al., 2013; Virgil et al., 2015) and include the following: (1) drawing of a reference line as drill-bits are recovered; (2) plaster pieces on bottom to mark the spatial position of a certain piece or section of the core; (3) geophysical imaging of the drilled hole, and (4) paleomagnetic re-orientation (e.g. Didenko, 1996; Virgil et al., 2015; Zhang et al., 2007). Paleomagnetic core re-orientation has been successfully used in hydrocarbon exploration projects defining fracture orientations confirmed by borehole image logging, mostly in sedimentary rocks (e.g. Alstine and Butterworth, 2002; Hailwood and Ding, 1995).

The Tolhuaca geothermal field (TGF, Melosh et al., 2010) is located on a tectonically active area of the southern Andean Volcanic Zone (Fig. 1a), south of the Callaqui-Copahue-Mandolegüe (CCM) first-order transfer zone (Fig. 1a). The CCM is a ENE-striking transitional zone regarding the nature of the rock basement, volcanism, and intra-arc tectonics (Fig. 1a) (e.g. Cembrano and Lara, 2009; Glodny et al., 2007; Melnick et al., 2006). The regional to local-scale fracture network in and around of the TGF is spatially associated with both the Liquiñe-Ofqui Fault System and the Andean Transverse Faults (ATF) (Cembrano and Lara, 2009; Melnick et al., 2006; Sanchez-Alfaro et al., 2016) (Fig. 1a). The LOFS includes a series of tens to hundred-kilometers long, subvertical NNE-striking master faults, NE-striking secondary faults and third order ENE-to-EW-striking faults, all cropping out from the area around the Callaqui volcano for about 1200 km south to the Golfo de Penas area (e.g. Cembrano et al., 2000; Lange et al., 2008; Veloso et al., 2009). The LOFS records a transpressional tectonic regime with a predominant dextral strike-slip deformation pattern (e.g. Lavenu and Cembrano, 1999; Pérez-Flores et al., 2016; Rosenau et al., 2006). This system is spatially and genetically associated with major stratovolcanoes (e.g. Copahue, Callaqui, Llaima, Lonquimay, Tolhuaca) and with shallow seismic activity (<25 km depth) (Fig. 1b) (Barrientos and Acevedo-Aránguiz, 1992; Lange et al., 2008; Legrand et al., 2011). The ATF includes a series of NW-striking structural elements – most probably inherited from a pre-Andean architecture (e.g. Radic, 2010) – with sinistral-reverse kinematics and local normal-slip re-activation (Pérez-Flores et al., 2016). These faults accommodate deformation driven by oblique convergence between Nazca and South America plates, with different kinematics depending of the preferential orientation of the fault-fracture network (Pérez-Flores et al., 2016). The transpressional regional tectonic regime, characterized by N65°E-trending σ_1 favors dextral/oblique displacement along NNE-striking faults, NE-ENE-striking extensional fractures and hybrid faults, and sinistral-reverse NW-striking faults (Lavenu and Cembrano, 1999; Pérez-Flores et al., 2016). Strain partitioning at these different tectonic domains control the chemistry of the volcanic products, the geometric and spatial arrangement of volcanic centers, as well as the hydrothermal activity in the intra-arc zone (Lara et al., 2006; Pérez-Flores et al., 2016; Radic, 2010; Sánchez et al., 2013; Sepúlveda et al., 2005; Sielfeld et al., 2016; Tardani et al., 2016).

Although these major faults have been widely recognized in the field at various scales, there is no published information on the subsurface distribution and orientation of structural elements in and around the TGF (Lohmar et al., 2012; Melosh et al., 2012, 2010). In this contribution, we report new structural data collected from a vertical, non-oriented, ca. 1080 m deep, borehole drilled in the NW flank of the Tolhuaca volcano (Tol-1). GeoGlobal Energy LLC kindly provided the Tol-1 drill core sampled during an exploration campaign held in 2012. We analyze standard mini-cores from the Tol-1 core using paleomagnetic techniques allowing the isolation of characteristic remanent magnetic vectors, thus providing a tool for the re-orientation of the drilled core. The orientation and characteristics of the local strain and stress fields of the TGF were then estimated with re-oriented fault-slip data.

2. Geological and tectonic framework

The Tolhuaca volcano is located at the intersection of the northern termination of the LOFS and a NW-striking fault of the ATF (Fig. 1a). Major structural elements present around of the volcanic edifice are spatially related to one of these faults, which could have provided a long-lived potential pathway for the ascent of deep-seated fluids (Pérez-Flores et al., 2016; Sanchez-Alfaro et al., 2016). Tolhuaca is a stratovolcano, which erupted both lava and pyroclastic flows, rising ca. 900 m above its basement – mostly Oligo-Miocene volcano-sedimentary rocks and Miocene granitic rocks of the Patagonian Batholith (Fig. 2) (Suárez and Emparan, 1997). Basaltic and basaltic-andesitic lava and pyroclastic flows, interbedded with andesite and dacite lava flows dominate the eruptive products (Lohmar et al., 2012; Melosh et al., 2012), which built up the volcanic edifice from at least ca. 290 ka (Ar-Ar method, Polanco et al., 2014). On the NW flank of Tolhuaca volcano two events of NW-striking fissural volcanism are dated to 160 ± 30 and 60 ± 30 ka (Ar-Ar method, Polanco et al., 2014), while the unglaciated NW-fissure and cone confirm volcanic activity after the last glaciation (<24.000 yr. B.P.) (Hulton et al., 2002; Kaplan et al., 2008; McCulloch et al., 2000). Nevertheless the Tolhuaca volcano has no record of historical eruptions (Lohmar et al., 2012; Suárez and Emparan, 1997; Thiele et al., 1987). At the NW-fissure location, there are several high-sulfur springs and fumaroles aligned on a NW-trending direction (e.g. Hauser, 1997; Melosh et al., 2010) suggesting the existence of one NW-striking fault that promotes the hydrothermal and magma ascent. Geochemical studies suggest the existence of a geothermal reservoir in this area with an estimated temperature of about 220°-300 °C (Melosh et al., 2010). These series of high-sulfur springs and fumaroles define the Tolhuaca Geothermal System (Fig. 2) (TGS; Melosh et al., 2010). The Lonquimay volcano, located 8 km to the south east of Tolhuaca volcano (Fig. 2), is an andesitic-basaltic stratovolcano built during the Upper-Pleistocene (mainly ca 100 ka; Polanco et al., 2014). The NE-flank of Lonquimay volcano consists of more than ten Holocene, NE-trending aligned, monogenetic cones (Polanco et al., 2014) with the last activity on the eruption of the Navidad cone in 1989. The radiometric ages record synchronous activity between the

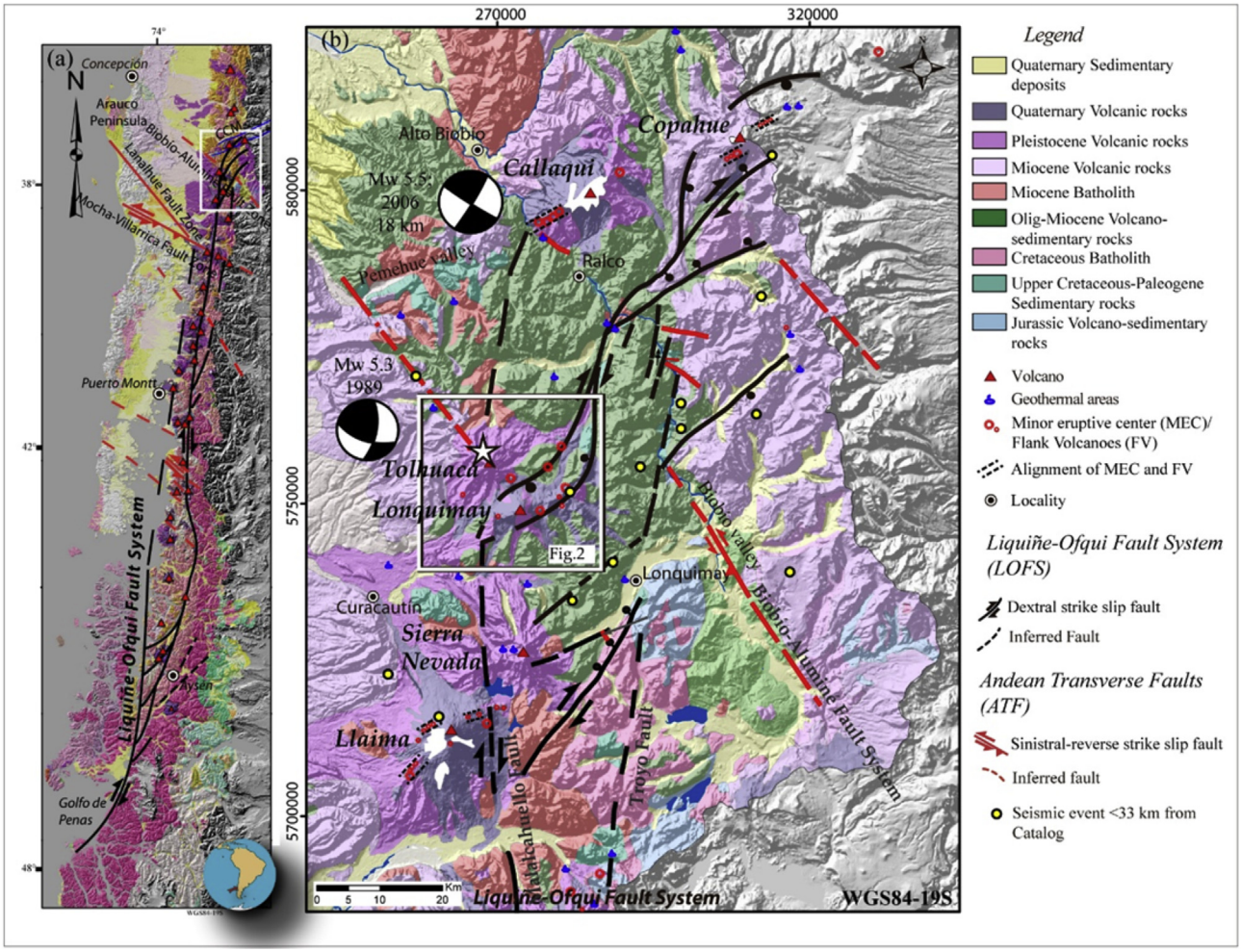

Fig. 1. (a) Composite Digital Elevation Model (DEM) and 1:1.000.000 geological map of the Southern Andes Volcanic Zone (Pérez-Flores et al., 2016; Sánchez et al., 2013) shows the study area (white square). Regional map showing the location and extent of the LOFS (black lines), ATF (red lines) and main Holocene volcanoes (red triangles). (b). Detailed map of the study area (white square on Fig. 1a) showing the main faults and lineaments of the LOFS and ATF (e.g. Biobío Aluminé Fault System), which are spatially and genetically associated with the Tolhuaca and the Lonquimay volcanoes, clusters of minor eruptive centers, hot springs and shallow seismicity (Barrientos and Acevedo-Aránguiz, 1992; Lange et al., 2008; Legrand et al., 2011). The white star shows the location of drill hole Tol-1, drilled by GeoGlobal Energy Chile (GGE Chile). (For interpretation of the references to colour in this figure legend, the reader is referred to the web version of this article.)

Lonquimay and Tolhuaca volcanoes (Polanco et al., 2014), using NE- and NW-striking fracture networks, respectively.

Regional to local-scale geometrical arrangements of faults, veins, and other structural elements of the LOFS develop in between two major NS-to-NNE-striking master faults linked by several NE-striking splays (Fig. 1b) (Melnick et al., 2006; Pérez-Flores et al., 2016; Rosenau et al., 2006). At the northernmost end of the LOFS (near the Tolhuaca, Callaqui and Lonquimay volcanoes) a series of *en echelon* NE-striking faults define a horse-tail geometry termination where a series of bends in the trace of these faults result in local dilatational jogs (e.g. Cembrano and Lara, 2009; Pérez-Flores et al., 2016; Rosenau et al., 2006). The Biobío-Aluminé Fault System is a blind sinistral-reverse fault which belongs to the ATF and is spatially associated with a linear NW-trending valley where it is possible to observe discrete fault outcrops (e.g. Melnick et al., 2006; Muñoz et al., 1988). The dextral strike-slip LOFS crosscuts and displaces the Biobío-Aluminé Fault System.

The Tolhuaca volcano is located on a NNE-striking master fault of the LOFS, close to a releasing bend defined by NE-striking faults at the Lonquimay volcano location. The extensional nature of the underlying NE-striking faults is documented by NE-aligned flank vents and a NE-striking fissure vent, both located at the NE-flank of the Lonquimay volcano (Fig. 2) (Pérez-Flores et al., 2016; Rosenau et al., 2006).

2.1. Tolhuaca geothermal system

Geothermal exploration campaigns including surface mapping, fluid geochemistry analyses, resistivity measurements and borehole logging have revealed the existence of a high enthalpy reservoir in the area (Lohmar et al., 2012; Melosh et al., 2010). Two slim holes (Tol-1 and Tol-2) and two larger diameter wells (Tol-3 and Tol-4) were drilled vertically down to 2117 m below surface. Tol-1 is the only one performed by diamond core drilling, with whole-rock recovery allowing for a detailed mineralogical and geometric analysis of faults, veins, and fractures. Temperature logging and analyses conducted on fluid sampling confirm the presence of a geothermal reservoir at ca. 1.5 km depth, at liquid-saturated conditions with temperatures up to 300 °C and a strong meteoric water component (Melosh et al., 2012). The main reservoir is overlain by a steam heated aquifer at shallow depths that reaches up to 160 °C of temperature (Melosh et al., 2012, 2010).

The Tol-1 borehole (Fig. 2) was cored through a thick pile of volcano-clastic deposits of mostly basaltic andesite composition.

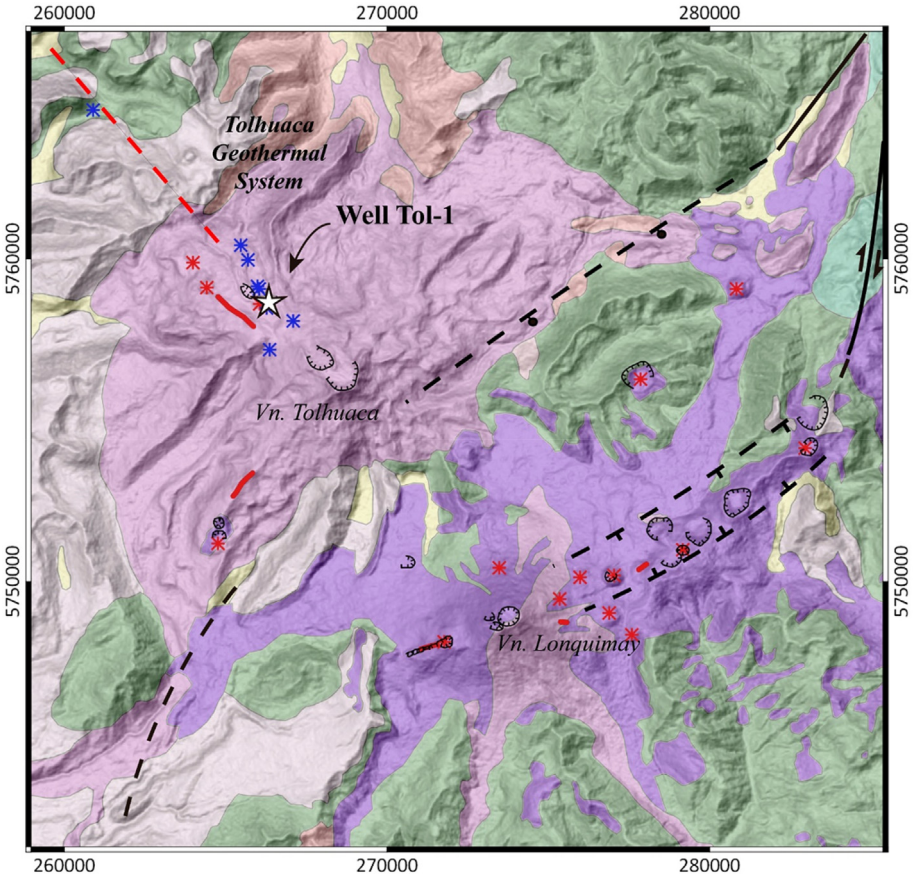

Fig. 2. Geological map at 1:100.000 scale (Suárez and Emparan, 1997) showing the Tolhuaca and Lonquimay volcanoes. The LOFS (black line) has been interpreted to form a dilatational jog geometry genetically associated with Lonquimay volcano and clusters of flank vents (red asterisk) (Pérez-Flores et al., 2016; Rosenau et al., 2006). Flank vents, fissures (red line) and fumarole areas (blue asterisk) are aligned in a NW trend (red dashed line) at the NW-flank of the Tolhuaca volcano, where the Tolhuaca Geothermal System (TGS) is located. See the legend in Fig. 1. (For interpretation of the references to colour in this figure legend, the reader is referred to the web version of this article.)

Predominant rock units correspond to lava flows and related breccia, volcanoclastic sediments, and minor tuff layers (see supplementary fig. SM1). Hyaloclastites and pillow breccia occur at different levels in the Tol-1 core, indicating eruptions in contact with glacial ice and/or water (Lohmar et al., 2012). A series of faults, joints, veins, and hydrothermal breccia are present all along the core (Fig. 3).

The alteration intensity is variable through the core, even at thin-section scale; the groundmass alteration is stronger than the phenocrysts. The following three main alteration zones are identified along the Tol-1 core: (1) shallow (<300 m depth) argillic characterized by clay minerals (smectite, interlayered chlorite-smectite), iron oxides and stilbite; (2) intermediate (300–670 m depth) sub-propylitic dominated by occurrence of interlayered chlorite-smectite and illite; and (3) deep (670–1073 m depth) propylitic alteration zones characterized by the occurrence of epidote and chlorite (Lizama et al., 2015; Sanchez-Alfaro et al., 2016). Mineralogy of argillic alteration records a temperature <200 °C (Lizama et al., 2015; Sanchez-Alfaro et al., 2016), while propylitic alteration forms in a broad range temperature between 200 and 350 °C (Reyes, 1990; Sanchez-Alfaro et al., 2016; Stimac et al., 2015). Mineralogical and geochemical studies (Lizama et al., 2015; Sanchez-Alfaro et al., 2016) of the TGS suggest that the system evolution is controlled by the interaction of mineralogical, hydrological and structural process segmented in depth, which affect the mechanical and hydrological properties of host-rock (Sanchez-Alfaro et al., 2016). In that sense, the clay-rich alteration zone (argillic zone) modifies the host-rock mechanical properties, promoting the generation/activation of shear faults and inhibiting highly permeable extensional fracturing (Sanchez-Alfaro et al., 2016). In contrast, in the deep up flow zone the less pervasive formation of clay mineral assemblages has allowed retention of rock strength and dilatant behavior during slip, sustaining high permeability conditions (Sanchez-Alfaro et al., 2016).

Sanchez-Alfaro et al. (2016) recognized four veins mineral paragenetic stages in the Tol-1 borehole. The paragenetic stages are present throughout Tol-1 with mineralogical variations. The earliest stage (S1) consists of a sequence of iron oxides (hematite), bands of amorphous silica and/or chalcedony and late pyrite with minor chalcopyrite. Clay mineral assemblages including smectite, minor interlayered chlorite-smectite, stilbite and epidote at depth dominate the stage S2, whereas calcite with lattice-bladed texture and quartz with various textures (euhedral, plumose, and microcrystalline) represent the stage S3. The S4 stage consists of microcrystalline quartz, amorphous silica phases and locally calcite, at deep propylitic zone by the occurrence of wairikite and late prehnite.

3. Methodology

3.1. Structural data collection and sampling

We measured a total of one hundred cm- and mm-scale structural elements – including faults, hybrid faults, veins, and breccia–

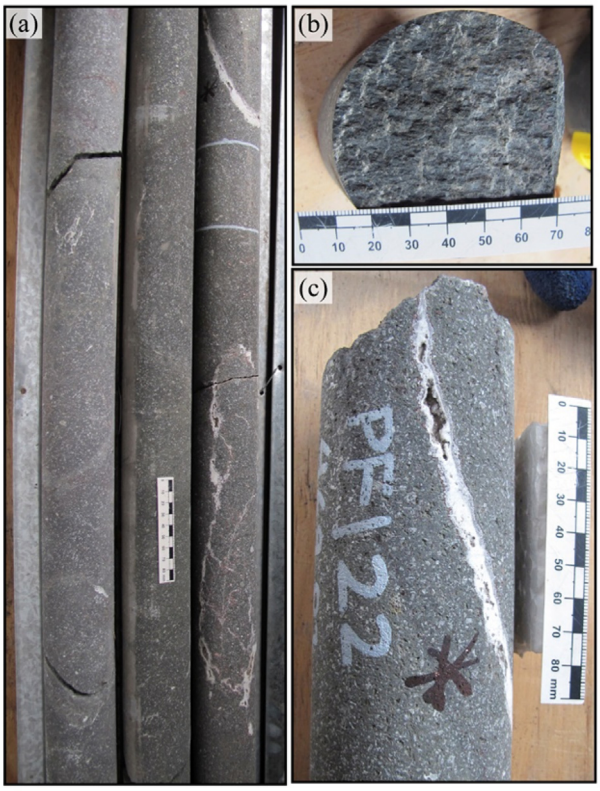

Fig. 3. Tol-1 coherent segment core of andesite (a) shows a vein and the spatially associated sample (white lines) used for paleomagnetic analysis. (b) Vertical view of the axis' core containing a fault plane with slickenlines; (c) side view of Tol-1 core including banded vein filled with quartz and zeolite.

recovered from the Tol-1 drill core (Fig. 3), taking as a reference frame the core axis and an arbitrary line drawn on the surface of the each recovered piece (Fig. 4). We drew an arbitrary reference line as perpendicular as possible to all structural elements present on the piece (or a coherent and adjacent series of them). Structural elements were only measured on pieces/sets of pieces longer than 40 cm, avoiding any possible rotation about an axis different from the axis of the core of the piece and therefore of the associated structural elements. The structural data collected include (Fig. 4): (1) the spatial orientation of a given structural element taken as a true dip (α_s) and relative strike (β_s, with respect to the reference line); (2) sense of movement (e.g. Doblas, 1998; Petit, 1987), (3) thickness in mm (ε), (4) mineral infill and (5) slickenfiber, striae and/or slickenline orientation (measured as a rake angle, ρ) (Fig. 4b, see mapping details at supplementary fig. SM1).

We collected two hundred standard paleomagnetic mini-cores (20 mm diameter and length), oriented by using their true inclination (α) and relative declination (β, with respect to the arbitrary reference line) (see supplementary fig. SM1; Fig. 4c). The mini-cores were collected in segments where the structural data was measured and sampled.

3.2. Paleomagnetic measurement

We demagnetized all mini-cores (Fig. 4c) by means of incremental temperature technique at the Petrofabrics and Paleomagnetics Laboratory of the University of Hawai'i at Manoa (SOEST-HIGP) using a MMTD-80 thermal demagnetizer. The demagnetization incremental steps were 50 °C from room temperature up to 600°-700 °C. We measured orientation and intensity of magnetic remanent (RM) vectors, at each step for all specimens, using the JR-5 Spinner Magnetometer. We used the "principal component analysis" of Kirschvink (1980) with the aid of Tauxe (1998)'s

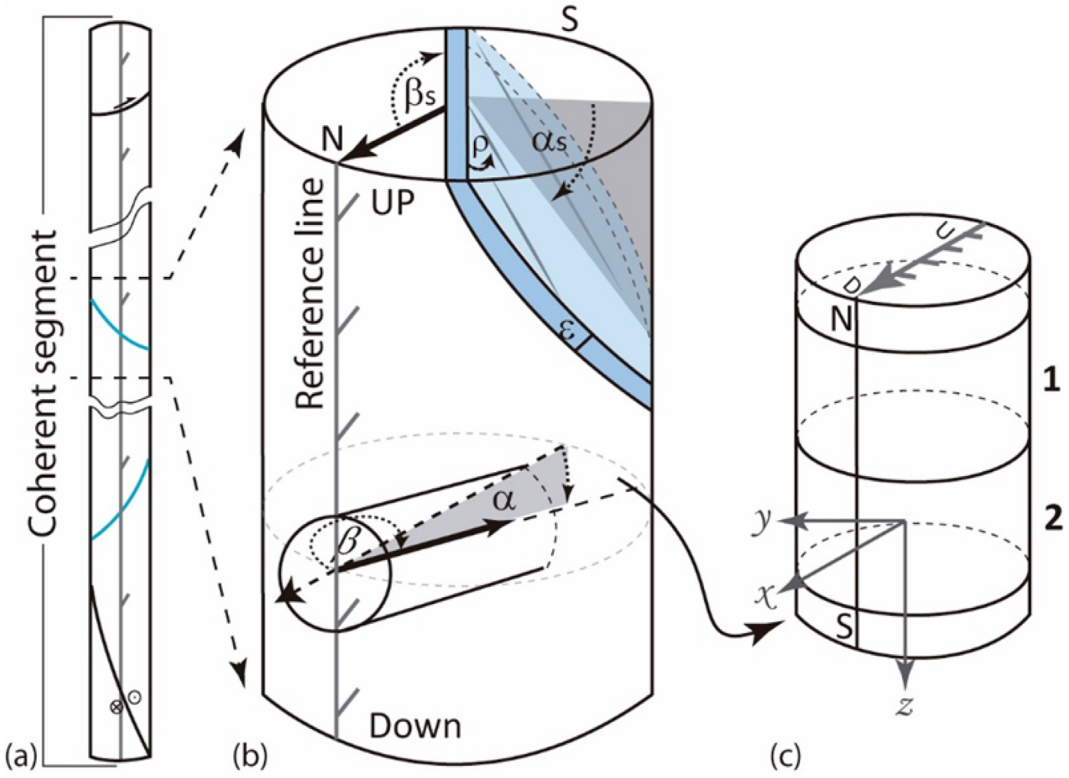

Fig. 4. Cartoon showing the sampling and structural measurement methodology. (a) For each coherent segment (or adjacent core pieces) containing structural elements, a reference line was drawn. (b) The spatial orientation of each structural element includes: (1) true dip (α_s) and relative strike (β_s, with respect to the reference line), (2) displacement direction, (3) thickness in mm (ε), (4) mineral infill and (5) orientation – measured as a rake angle (ρ) – of the striae, slickenline and mineral fiber. (c) A standard paleomagnetic mini-coring oriented by their true plunge (α) and relative trend (β, with respect to the arbitrary reference line) was measured for each coherent segment.

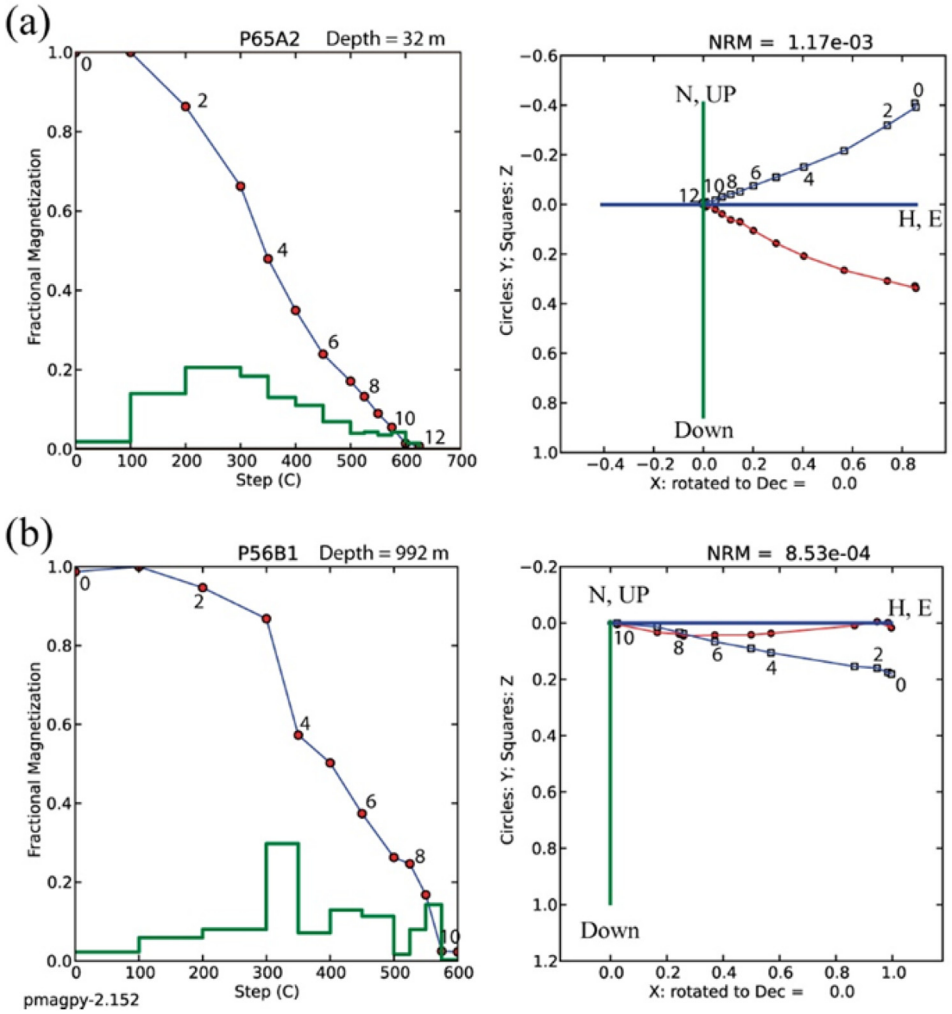

Fig. 5. Results of progressive thermal demagnetization of representative samples, from 32 m (a) and 992 m (b) depth, displayed by partial demagnetization graphic (left wards) and vector end point diagrams (right wards) (Zijderveld, 1967). For Zijderveld diagrams, each data point represents the projection of the magnetization vector for individual demagnetization steps onto the horizontal (red circle solid symbols) and vertical (blue square open symbols) plane. Numbers adjacent to data points indicate the demagnetization step (leftwards). Sample number, sample depth and NRM intensity are shown at the top of each diagram. Data shown in core coordinates. (For interpretation of the references to colour in this figure legend, the reader is referred to the web version of this article.)

PMagPy routines for the orientation of ChRM vectors from the demagnetization paths of each specimen. ChRM vectors with MAD (maximum angular deviation) values larger than 15° are ill-defined and therefore rejected for further analyses (e.g. Butler, 1998).

We rotated each individual ChRM vector declination about a vertically oriented axis to fit to a determined reference frame. The reference frame corresponds to the orientation of the Geocentric Axial Dipole (GAD) model (000°, −57.7°) (Butler, 1998) calculated for the Tolhuaca area (38.29°S and 71.67°W). It is worth noticing that this reference frame assumes that no rotation affected the Tol-1 site since, at least, the age of the deepest drilled lava flow (i.e. < 1 My Lohmar et al., 2012). The fitting procedure of NRM vectors declination data to the reference frame provided the rotational declination angle for each individual (set of) piece. We rotated piece by piece, and hence the measured structural data using the rotational declination angle.

3.3. Structural data analysis

We determined the orientation of strain and stress fields from the kinematic and dynamic analysis of the re-oriented fault-slip data. The average orientation of the P (shortening) and T (stretching) axes (e.g. Marrett and Allmendinger, 1990) calculated for each fault allows to estimate the orientation of the strain field. These axes restrict on space the orientation of both shortening and stretching quadrants. We estimated the orientation of the principal stress axes through the "Multiple Inverse Method" (e.g. Yamaji, 2000) using the stress regimes defined by Ritz (1994) as tensional, compressional or strike-slip. The method estimates a best-fit stress tensor for each of all possible subpopulations drawn from the entire structural data. Best-fit tensor solutions are then plotted on separate stereonets – one for σ_1 and other for σ_3 – using a color-coded symbol according to its stress ratio ($\varphi = \sigma_2\text{-}\sigma_3/\sigma_1\text{-}\sigma_3$) and with an attached tail pointing towards the orientation of the complementary axis (i.e. tail on σ_1 points towards σ_3). Common stress field solutions are seen as clusters of sub-solutions with similar colors and with their tails pointing towards a common orientation (e.g. Otsubo et al., 2006; Yamaji, 2000). Thus, for the obtained stress field, the difference between observed and theoretical slip direction obtained corresponds to the misfit angle. The solution with more activated faults with misfit angles less than 30° is the stress axes orientation solution.

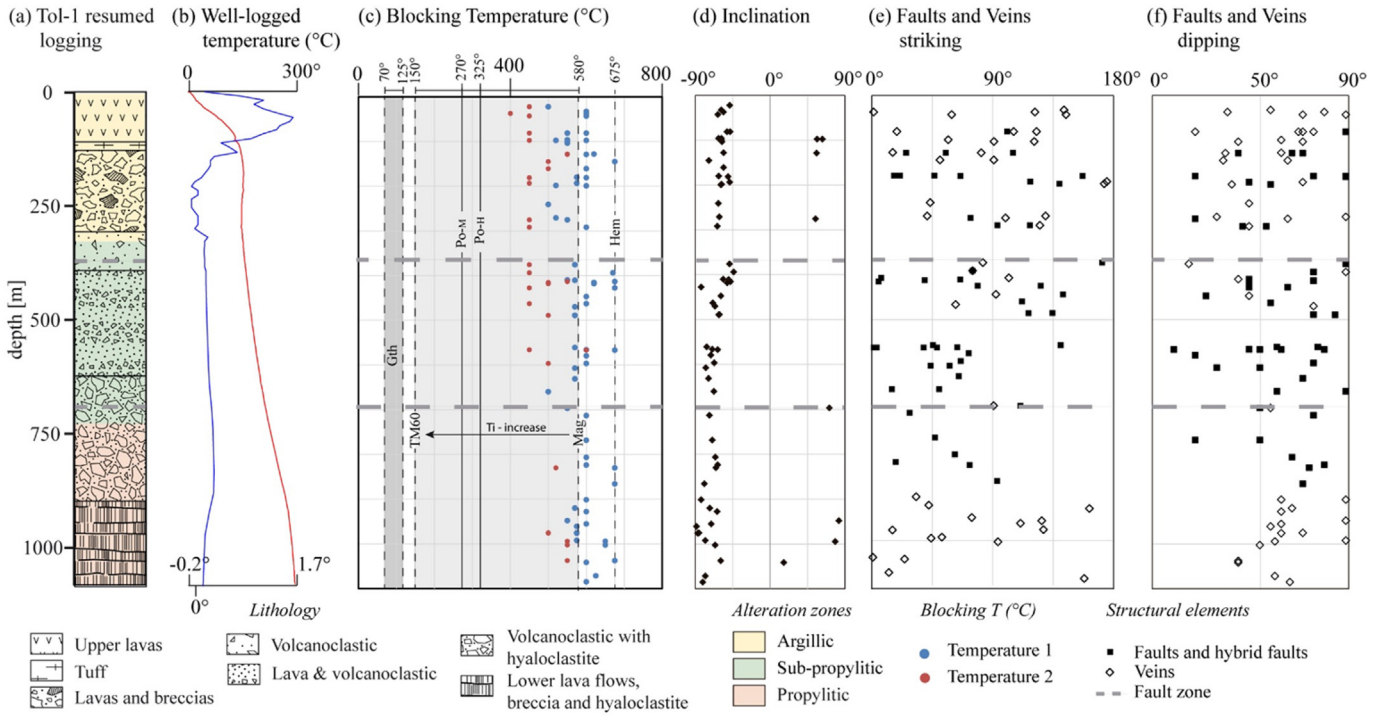

Fig. 6. (a) General lithological and alteration zones logging of the borehole Tol-1 (Sanchez-Alfaro et al., 2016) (see supplementary figure SM1). (b) Temperature (°C) (red line) and temperature gradient (blue line) vs. depth profile for the Tol-1 (Sanchez-Alfaro et al., 2016). (c) Blocking temperatures vs. depth for each specimen. Blocking temperatures showed for key minerals as a reference: goethite (Gth), pyrrhotite monoclinic (Po-M) and hexagonal (Po-H), hematite (Hem) and magnetite (Mag) with variation of titanium composition until titanomagnetite containing 60 mol% Ti (TM60) (Whitney and Evans, 2010). (d) Inclination of remanent magnetization vectors, (e) faults and veins striking and (f) dipping variation through the depth of Tol-1 borehole. (For interpretation of the references to colour in this figure legend, the reader is referred to the web version of this article.)

4. Results

Fig. 6 shows the general lithologies and alteration zones identified along of Tol-1 core (Fig. 6a) and temperature/gradient (°C) profile measured (Fig. 6b). This information contextualizes into the Tol-1 core geology the paleomagnetic and structural results.

4.1. Demagnetization patterns and RM vectors (Table 1)

Natural remanent magnetization (NRM) intensities (prior to thermal demagnetization) are variable, ranging from 10.6 to 34.9 $\times$ 10^3 mA/m. Thermal demagnetization vector patterns are stable with incremental demagnetization steps going towards the origin on a nearly linear trajectory from the beginning to the end of the core (Fig. 5a and b). The fractional thermal remanent demagnetization (Fig. 5) allows calculating the blocking temperatures of magnetic signal carrying on minerals of each mini-core along the Tol-1 core (Fig. 6c). The bulk of demagnetization occurs in the range 400°–675 °C (Fig. 6c), suggesting the presence of magnetite, with varying Ti-content, as the principal remanence carrier. Magnetization left after demagnetization at >645 °C suggest minor amounts of hematite (Fig. 6c).

NRM vectors record inclinations mainly between −80° and −50° (Fig. 6d) yet eight samples yielded positive inclinations. The local normal polarity field inclination, defined by GAD model, is −58°. Samples yielding normal polarity inclinations are, within statistical error, close to the theoretical GAD inclination (−57.7 ± 20°) (e.g. Butler, 1998; Tauxe, 1998) for the Tol-1 borehole latitude. The inclinations of NRM vectors recorded along to the Tol-1 core are mainly normal polarity. We did not find any continuous break from normal (- inclination) to reverse (+inclination) polarity, but instead peaks on where sudden and short polarity changes occur. Scattered reverse polarity specimens could record polarity excursions or errors due to incorrect up/down assessment in the core segments. The origin of these reverse polarities need to be tested so that we decide to reject these samples and its associated structural data.

4.2. Structural elements on Tol-1 borehole (see details in supplementary fig. SM1 and Table 2)

Detailed mapping of the Tol-1 borehole identifies 93 mesoscopic-scale veins and faults (supplementary fig. SM1). Reoriented structures show a slight NE- and NW-striking preferential orientation. We recognized two major fault zones at 310 m and 660 m (with 50 cm and 40 cm of gouge, respectively); their precise orientation was not possible to obtain because of their irregular boundary. These fault zones are spatially associated with alteration zones boundaries (Fig. 6a). The reoriented structural elements show a wide distribution of strike and dip throughout the core (Fig. 6d and e). We recognized three zones with contrasting faults and veins patterns (strike and dip) and hydrothermal alteration mineral assemblages. There is a shallow (above 450 m depth) zone, where faults and veins are filled with one or more of the following minerals: Fe-oxides, calcite, quartz, silica, chalcedony, zeolite and chlorite/smectite. Mineral assemblages indicate an argillic alteration type. Breccia textures are typically found at the bottom of this structural-mineralogical zone. Faults and veins in the shallow zone display a wide range of strikes and dips. Faults and hybrid faults filled with calcite, quartz, chalcedony, chlorite/smectite and less common Fe-oxide, zeolite, silica, and magnetite dominate the intermediate (400–700 m) zone, indicating a propylitic alteration type. Faults orientation predominantly are NNE-ENE-striking and >50° dipping. Finally, veins filled with epidote, calcite, zeolite,

Table 1
Paleomagnetic sampling information and thermal demagnetization results showing: N, steps number; T. min/T. max, temperature (°C) minimum and maximum; MAD, maximum angular deviation; declination/inclination in sample coordinate and RM vectors in geographic coordinate used by fault and veins reorientation.

Sampling information							Demagnetization						RM vector (Geographic Coordinate)	
Sample	Lithology	Aleteration	Trend	Hade	Plunge	Depth	N	T. min	T. max	MAD	Declination	Inclination	Declination	Inclination
P63A2	Andesite flow interior	Unalterated	183	87.5	2.5	22.25	7	100	500	2.4	35.6	19.6	239.1	−48.6
P65A2	Amygdaloidal andesite. Flow Breccia	Unalterated	184	90.5	−0.5	32.57	11	100	600	3.7	22.1	−22.2	321.9	−58.7
P66B2	Amygdaloidal andesite. Flow Breccia	Argillic	191	87.5	2.5	37.2	10	100	575	3.8	29.2	15.2	248.6	−56.1
P64B1	Amygdaloidal andesite. Flow Breccia	Argillic	184	89.5	0.5	42.82	10	100	575	3.2	10.6	24.6	205.5	−62.9
P1B1	Andesite flow interior	Argillic	179	81	9	81.03	8	200	550	4.5	336.2	21.2	141.5	−51.8
P1B2	Andesite flow interior		179	82	8	81.03	5	200	450	2.5	340.5	29.4	153.2	−48.2
P2C1	Andesite flow interior	Argillic	194	87	3	96.02	8	300	575	6.6	332.6	−9.5	89.3	−62
P2C2	Andesite flow interior		194	87	3	96.02	9	200	575	4	336.2	17.9	146.6	−58.6
P3A2	Andesite flow interior	Argillic	183	88.5	1.5	97.33	11	0	575	3.9	156.9	16.5	238.3	62.8
P3B1	Andesite flow interior		183	90	0	97.33	7	200	525	8.9	153.1	20.8	233	56.5
P4B1	Andesite flow interior	Argillic	200	89	1	99.39	6	350	550	1.5	334.6	17.8	148.1	−58.7
P5A2	Andesite flow interior	Argillic	185	89	1	103.39	11	0	550	4.5	328.5	−4	89.1	−57.9
P6A2	Amygdaloidal andesite. Flow interior	Argillic	187	88.5	1.5	128.05	13	0	625	2	24.2	23	229.4	−56
P7A2	Amygdaloidal andesite. Flow interior	Argillic	186	88.5	1.5	128.82	12	0	600	2.7	209.1	20.3	131.5	55.9
P8A2	Amygdaloidal andesite. Flow interior	Argillic	175	91	−1	145	11	200	675	2.3	13.5	10.5	229.2	−73.6
P9B2	Andesite flow breccia	Sub-propylitic	187	87	3	160.64	14	0	650	3	34	−6.2	283.6	−56
P10A2	Andesite flow interior	Argillic	233	90.5	−0.5	180	11	200	625	1.9	23.1	−16.3	0.4	−61.7
P11A2	Andesite flow interior	Argillic	188	87.5	2.5	181.05	9	200	575	2.8	12.4	35.3	204	−50.5
P12B2	Andesite flow interior	Argillic	182	90	0	193.42	7	300	600	2.6	321.8	−17.4	65.1	−48.6
P13A2	Andesite flow interior	Argillic	176	90	0	199.19	10	100	575	3.3	333.5	16.3	119.2	−59.2
P14A2	Andesite flow interior	Argillic	227	88	2	198.45	8	100	525	3.3	328.7	−8.5	124	−58.2
P15A2	Andesite-basaltic, flow interior	Argillic	173	90	0	240.65	9	200	575	2.3	13.3	−24.8	326.5	−62.1
P16A2	Andesite-basaltic, flow interior	Argillic	183	91	−1	270.82	7	200	525	3.8	17.2	24.7	216.7	−61
P17A2	Andesite-basaltic, flow interior	Sub-propylitic	193	87	3	275.14	6	100	450	3.5	178.9	38.4	194.5	54.6
P18A2	Andesite-basaltic, flow interior	Sub-propylitic	198	86	4	291.8	8	300	575	6.3	1.6	−30.6	14.9	−63.4
P19A1	Andesite-basaltic, Breccia	Sub-propylitic	172	91	−1	298.4	–	–	–	–	–	–	–	–
P20B1	Andesite flow interior	Sub-propylitic	184	89	1	375.7	9	200	575	5.6	39	13.3	252.3	−48.8
P21B1	Andesite flow breccia	Sub-propylitic	179	92.5	−2.5	393.84	13	200	675	5.4	16.7	46.3	195	−43.8
P22B1	Andesite flow breccia	Sub-propylitic	180	89	1	410.51	11	0	575	6.3	350.8	38.3	167.7	−49.9
P23B2	Andesite flow breccia	Sub-propylitic	194	88.5	1.5	409.82	10	0	550	8	344.2	28.8	168	−56.3
P24A2	Andesite flow breccia	Sub-propylitic	179	92	−2	413.2	13	200	675	4.5	326.7	28.6	132.2	−48.6
P25A2	Andesite flow breccia	Sub-propylitic	172	90	0	415.4	9	350	625	1.8	317.7	−1	80.5	−47.7
P26A2	Andesite flow breccia	Sub-propylitic	178	84.5	5.5	417.86	11	200	625	4.1	28	21.2	222.9	−51.7
P27A2	Volcanoclastic andesite, Tuff	Sub-propylitic	184	88.5	1.5	427.58	12	300	675	5.3	353.4	1.2	116.2	−82.9
P28B1	Andesite flow interior	Sub-propylitic	181	88	2	447	13	0	625	3.9	347.9	−30.6	21.6	−59.2
P29B1	Andesite-basaltic, flow interior	Sub-propylitic	188	86.5	3.5	462.7	15	0	675	1.7	16.7	−16.8	318.2	−68.9
P30B1	Andesite-basaltic, flow interior	Sub-propylitic	183	88.5	1.5	469.75	9	200	575	3	337.7	4	107.6	−66.2
P31A2	Andesite-basaltic, flow interior	Sub-propylitic	177	94.5	−4.5	488.9	8	300	575	3.4	339.5	−16.5	40.5	−60.8
P32A2	Andesite-basaltic, flow interior	Sub-propylitic	189	89.5	0.5	489.21	7	350	575	3	336.4	−16.5	63.3	−61.8
P33B1	Andesite flow interior	Sub-propylitic	182	91	−1	560.91	10	100	575	3.1	9.4	11.1	224.4	−76.2
P34A1	Andesite flow breccia	Sub-propylitic	173	86.5	3.5	566.1	11	200	625	5.6	14.2	11.4	216.3	−69.5
P35B	Andesite flow breccia	Sub-propylitic	177	87	3	566.68	13	200	675	4.3	7.2	23.9	191.4	−63.1
P36B	Pillow Breccia and Hyaloclastite Andesite	Sub-propylitic	169	90	0	579.32	11	200	625	2.1	15.3	10.9	222.9	−71.3
P37B1	Andesite flow interior	Sub-propylitic	180	87.5	2.5	596.55	12	100	625	3.5	339.9	8.4	118.7	−67.2
P38B1	Andesite flow interior	Sub-propylitic	186	88	2	607.07	9	200	575	2.4	5.3	−13.7	342.1	−77.2
P39B1	Volcanoclastic andesite, Tuff	Sub-propylitic	178	91.5	−1.5	630.77	10	100	575	4.8	352.6	−12.6	25.3	−74.1
P40B1	Volcanoclastic andesite, Tuff	Sub-propylitic	185	88	2	659.6	8	0	500	9.2	4.2	−24.1	354.9	−67.5
P41B1	Volcanoclastic andesite, Tuff	Sub-propylitic	181	88	2	696.68	9	100	550	4.6	172.2	19.3	204.3	71.1
P42B1	Volcanoclastic andesite, Tuff	Sub-propylitic	181	92.5	−2.5	713.01	12	0	600	4.1	343.2	−0.3	81.8	−73
P43B1	Volcanoclastic andesite, Tuff	Propylitic	181	90	0	768.1	10	200	600	6.3	14.1	15.2	222.9	−69.4
P44B	Volcanoclastic andesite, Tuff	Propylitic	181	90	0	806.35	8	200	550	4.3	350.4	−22.3	23.1	−65.8
P45B1	Volcanoclastic andesite	Propylitic	180	89	1	823.53	9	200	575	5.7	18.8	18.7	222.2	−63
P46B	Volcanoclastic andesite	Propylitic	184	90.5	−0.5	829.95	9	200	575	4.2	18.2	17.7	229.1	−65.2
P47B	Volcanoclastic andesite	Propylitic	180	90.5	−0.5	865.62	10	100	575	3.1	9.8	5.7	241.8	−78.9
P48B	Volcanoclastic andesite	Propylitic	182	92	−2	901.17	5	200	600	4.4	355	−3.33	47	−82.9
P49B	Andesite flow interior	Propylitic	181	88.5	1.5	920.1	10	100	575	5.5	352.9	14.5	157.5	−72.5
P50B1	Andesite flow interior	Propylitic	181	89	1	927.78	6	400	600	5.3	21	15.3	232	−63.6
P51B1	Andesite flow interior	Propylitic	179	90	0	947.89	11	100	600	10.4	182.7	−6.8	20.6	82.7
P52B1	Andesite flow interior	Propylitic	194	88.5	1.5	955.34	13	0	625	8	340.8	−3.9	96.5	−70.7
P53B1	Andesite flow interior	Propylitic	177	90	0	960.83	11	0	575	9.2	1	1.1	219.3	−88.5
P54B	Andesite flow interior	Propylitic	193	88.5	1.5	975.31	11	0	575	10	356.5	−4.3	64.2	−85.5
P55B1	Andesite flow interior	Propylitic	181	91	−1	976.06	10	100	575	12.2	359.5	4	171.6	−87
P56B1	Andesite flow interior	Propylitic	178	88.5	1.5	992.12	12	0	600	2.9	358.9	10.5	172.8	−78
P57B	Andesite flow interior	Propylitic	177	88.5	1.5	994.32	14	0	650	5.6	190.8	−2.7	65.8	78.4
P58B1	Andesite flow interior, breccia	Propylitic	184	92.5	−2.5	1002.43	8	450	650	5.7	348.7	−18.8	31.1	−66
P59A	Pillow Breccia and Hyaloclastite Andesite	Propylitic	179	88.5	1.5	1037.55	13	200	675	6	13	26.5	202.2	−59.3
P60B	Pillow Breccia and Hyaloclastite Andesite	Propylitic	172	90	0	1041.51	4	525	600	3.8	106.5	8.1	253.6	16.3
P61B	Andesite flow interior, breccia	Propylitic	183	88.5	1.5	1071.49	14	100	675	8.1	12.2	−3.8	280.3	−77.9
P62A1	Andesite flow interior, breccia	Propylitic	193	90	0	1084.96	13	0	625	9.5	8.6	2.8	264.9	−81

Table 2
Geological-structural mapping.

Lithology	Alteration	Strike	Strike 0–90 (Graph)	Dip Dir	Dip	Rake	Type	Sense of slip	Fe-ox	Cal	Zeo	Prh	Silica	Chal	Qz	Chl/sme	Mag	Py	Ep	Width (mm)	Depth
Amygdaloidal andesite. Flow Breccia	Unalterated	143.1	143.1	233.1	55	–	V		x											5	32.57
Amygdaloidal andesite. Flow Breccia	Argillic	1.4	1.4	91.4	80	–	V		x	x			x	x						7	37.2
Amygdaloidal andesite. Flow Breccia	Argillic	121.4	121.4	211.4	35	–	V		x											5	37.2
Amygdaloidal andesite. Flow Breccia	Argillic	239.5	59.5	329.5	90	–	V		x											6	42.82
Amygdaloidal andesite. Flow Breccia	Argillic	144.5	144.5	234.5	70	–	V		x											4	42.82
Andesite flow interior	Argillic	297.7	117.7	27.7	75	30	F	NL	x	x										0.5	81.03
Andesite flow interior	Argillic	302.7	122.7	32.7	70	–	V		x	x										0.5	81.03
Andesite flow interior	Argillic	302.7	122.7	32.7	68	–	V		x	x										0.5	81.03
Andesite flow interior	Argillic	198.7	18.7	288.7	75	–	V		x	x										4	81.03
Andesite flow interior	Argillic	285.7	105.7	15.7	20	–	V		x											0.5	81.03
Andesite flow breccia	Argillic	56.9	56.9	146.9	60	–	V		x	x	x		x	x					x	5	99.39
Andesite flow breccia	Argillic	90.9	90.9	180.9	70	–	V		x	x	x		x						x	10	103.39
Andesite flow breccia	Argillic	120.9	120.9	210.9	40	–	V		x											6	103.39
Amygdaloidal andesite. Flow interior	Argillic	15.6	15.6	105.6	60	–	V		x											3	128.05
Amygdaloidal andesite. Flow interior	Argillic	273.5	93.5	3.5	20	133	F	TL	x	x										1	128.82
Amygdaloidal andesite. Flow interior	Argillic	351.5	171.5	81.5	50	130	F	NR	x	x										4	128.82
Amygdaloidal andesite. Flow interior	Argillic	261.5	81.5	351.5	34	–	V		x											6	128.82
Amygdaloidal andesite. Flow interior	Argillic	73.5	73.5	163.5	65	62	F	–	x	x										2	128.82
Amygdaloidal andesite. Flow interior	Argillic	90.8	90.8	180.8	63	–	V		x	x										12	145
Amygdaloidal andesite. Flow interior	Argillic	50.8	50.8	140.8	33	–	V		x											1	145
Andesite flow interior	Argillic	319.6	139.6	49.6	80	110	F	NR	x	x										1	180
Andesite flow interior	Argillic	196.6	16.6	286.6	73	110	F	NR	x	x										1	180
Andesite flow interior	Argillic	46.6	46.6	136.6	70	55	F	–	x	x										1	180
Andesite flow interior	Argillic	201.0	21.0	291.0	75	63	F	NR	x	x										0.5	181.05
Andesite flow interior	Argillic	246.0	66.0	336.0	85	108	F	–	x	x	x									0.5	181.05
Andesite flow interior	Argillic	156.9	156.9	246.9	58	90	F	NR	x	x										2	193.42
Andesite flow interior	Argillic	354.9	174.9	84.9	70	–	V		x											3	193.42
Andesite flow interior	Argillic	298.0	118.0	28.0	77	54	F	NL	x	x				x						1	198.45
Andesite flow interior	Argillic	173.0	173.0	263.0	37	–	V		x	x										1	198.45
Andesite-basaltic, flow interior	Argillic	43.5	43.5	133.5	45	–	V			x				x						1	240.65
Andesite-basaltic, flow interior	Argillic	221.3	41.3	311.3	90	–	V			x					x					2	270.82
Andesite-basaltic, flow interior	Argillic	309.3	129.3	39.3	30	–	V		x											25	270.82
Andesite-basaltic, flow interior	Argillic	279.5	99.5	9.5	63	–	V		x	x			x	x	x					10	275.14
Andesite-basaltic, flow interior	Argillic	205.5	25.5	295.5	45	105	F	–	x	x						x				2	275.14
Andesite-basaltic, flow interior	Sub-propylitic	305.1	125.1	35.1	45	–	V		x	x					x					15	291.8
Andesite-basaltic, flow interior	Sub-propylitic	105.1	105.1	195.1	60	45	F	NL	x							x				1	291.8
Andesite-basaltic, flow interior	Sub-propylitic	235.1	55.1	325.1	10	140	F	–	x							x				5	291.8
Andesite flow interior	Sub-propylitic	100.7	100.7	190.7	80	120	F	–		x										1	375.7
Andesite flow interior	Sub-propylitic	82.7	82.7	172.7	17	–	F													0	375.7
Andesite flow breccia	Sub-propylitic	75.0	75.0	165.0	50	32	F	NR		x										1	393.84
Andesite flow breccia	Sub-propylitic	75.0	75.0	165.0	90	–	V		x	x				x	x					50	393.84
Andesite flow breccia	Sub-propylitic	282.0	102.0	12.0	40	–	V		x	x				x	x		x			4	409.82
Andesite flow breccia	Sub-propylitic	7.0	7.0	97.0	20	67	F	NL	x	x				x	x	x				1	409.82
Andesite flow breccia	Sub-propylitic	65.8	65.8	155.8	75	20	F	TR		x										2	413.2
Andesite flow breccia	Sub-propylitic	39.5	39.5	129.5	50	40	F	–												2	415.4
Andesite flow breccia	Sub-propylitic	5.1	5.1	95.1	30	90	F	TL		x										1	417.86
Volcanoclastic andesite, Tuff	Sub-propylitic	125.8	125.8	215.8	70	65	F	NL												0	427.58
Volcanoclastic andesite, Tuff	Sub-propylitic	258.8	78.8	348.8	90	165	F	NR												0	427.58
Andesite flow interior	Sub-propylitic	92.4	92.4	182.4	45	–	V						x		x	x				5	447
Andesite flow interior	Sub-propylitic	322.4	142.4	52.4	58	70	F	–		x										1	447
Andesite-basaltic, flow interior	Sub-propylitic	291.8	111.8	21.8	50	80	F	NL	x	x										1	462.7
Andesite-basaltic, flow interior	Sub-propylitic	242.4	62.4	332.4	75	–	V		x	x	x			x	x	x				15	469.75
Andesite-basaltic, flow interior	Sub-propylitic	314.5	134.5	44.5	25	90	F	TL		x						x				1	488.9
Andesite-basaltic, flow interior	Sub-propylitic	116.7	116.7	206.7	55	65	F	–	x											1	489.21
Andesite flow interior	Sub-propylitic	320.6	140.6	50.6	45	105	F	TL	x	x					x	x				1	560.91
Andesite flow interior	Sub-propylitic	225.6	45.6	315.6	75	160	F	–		x										1	560.91

Andesite flow breccia	Sub-propylitic	243.7	63.7	333.7	45	128	F	NR		x									1	566.1
Andesite flow breccia	Sub-propylitic	183.6	3.6	273.6	45	167	F	–		x									2	566.68
Andesite flow breccia	Sub-propylitic	1.6	1.6	91.6	45	70	F	NL											1	566.68
Andesite flow breccia	Sub-propylitic	38.6	38.6	128.6	63	10	F	TR											1	566.68
Andesite flow breccia	Sub-propylitic	228.6	48.6	318.6	75	170	F	TL											2	566.68
Pillow Breccia and Hyaloclastite Andesite	Sub-propylitic	252.1	72.1	342.1	53	130	F	–	x	x	x			x	x	x		x	1	579.32
Andesite flow interior	Sub-propylitic	66.3	66.3	156.3	42	100	F	NR		x									1	596.55
Andesite flow interior	Sub-propylitic	57.9	57.9	147.9	90	5	F	TR	x	x					x	x			5	607.07
Andesite flow interior	Sub-propylitic	43.9	43.9	133.9	20	100	F	–	x										2	607.07
Volcanoclastic andesite, Tuff	Sub-propylitic	64.7	64.7	154.7	55	15	F	–											1	630.77
Volcanoclastic andesite, Tuff	Sub-propylitic	195.1	15.1	285.1	75	45	F	–		x									1	659.6
Volcanoclastic andesite, Tuff	Sub-propylitic	50.1	50.1	140.1	90	40	F	NL											1	659.6
Volcanoclastic andesite, Tuff	Sub-propylitic	290.7	110.7	20.7	20	150	F	NR		x									1	696.68
Volcanoclastic andesite, Tuff	Sub-propylitic	270.7	90.7	0.7	55	–	V			x									6	696.68
Volcanoclastic andesite, Tuff	Sub-propylitic	28.2	28.2	118.2	90	65	F	TR		x							x	x	3	713.01
Volcanoclastic andesite, Tuff	Propylitic	47.1	47.1	137.1	90	45	F	TR		x	x				x	x	x	x	5	768.1
Volcanoclastic andesite, Tuff	Propylitic	47.1	47.1	137.1	45	100	F	NR											1	768.1
Volcanoclastic andesite, Tuff	Propylitic	61.9	61.9	151.9	40	105	F	–		x									5	806.35
Volcanoclastic andesite	Propylitic	17.8	17.8	107.8	70	140	F	NR		x							x		1	823.53
Volcanoclastic andesite	Propylitic	72.9	72.9	162.9	65	90	F	NR		x					x				3	829.95
Volcanoclastic andesite	Propylitic	273.2	93.2	3.2	90	85	F	–		x					x			x	15	865.62
Volcanoclastic andesite	Propylitic	33.0	33.0	123.0	90	–	V			x								x	5	901.17
Volcanoclastic andesite	Propylitic	213.0	33.0	303.0	60	–	V			x					x	x	x	x	4	901.17
Andesite flow interior	Propylitic	42.5	42.5	132.5	65	–	V			x								x	1	920.1
Andesite flow interior	Propylitic	162.0	162.0	252.0	60	–	V			x								x	1	927.78
Andesite flow interior	Propylitic	254.4	74.4	344.4	90	–	V				x	x		x			x	x	1	947.89
Andesite flow interior	Propylitic	306.5	126.5	36.5	60	–	V								x			x	3	955.34
Andesite flow interior	Propylitic	110.7	110.7	200.7	55	–	V			x					x				4	960.83
Andesite flow interior	Propylitic	307.8	127.8	37.8	70	–	V			x	x	x		x	x	x		x	6	975.31
Andesite flow interior	Propylitic	195.4	15.4	285.4	60	–	V			x					x			x	2	976.06
Andesite flow interior	Propylitic	232.2	52.2	322.2	90	–	V				x	x		x	x		x		5	992.12
Andesite flow interior	Propylitic	224.2	44.2	314.2	57	–	V								x				6	994.32
Andesite flow interior, breccia	Propylitic	93.9	93.9	183.9	50	–	V				x				x				1.5	1002.43
Pillow Breccia and Hyaloclastite Andesite	Propylitic	0.8	0.8	90.8	40	–	V				x				x				20	1037.55
Pillow Breccia and Hyaloclastite Andesite	Propylitic	24.4	24.4	114.4	40	–	V			x					x				5	1041.51
Andesite flow interior, breccia	Propylitic	192.7	12.7	282.7	57	–	V			x	x			x	x	x		x	5	1071.49
Andesite flow interior, breccia	Propylitic	158.1	158.1	248.1	64	–	V			x					x			x	22	1084.96

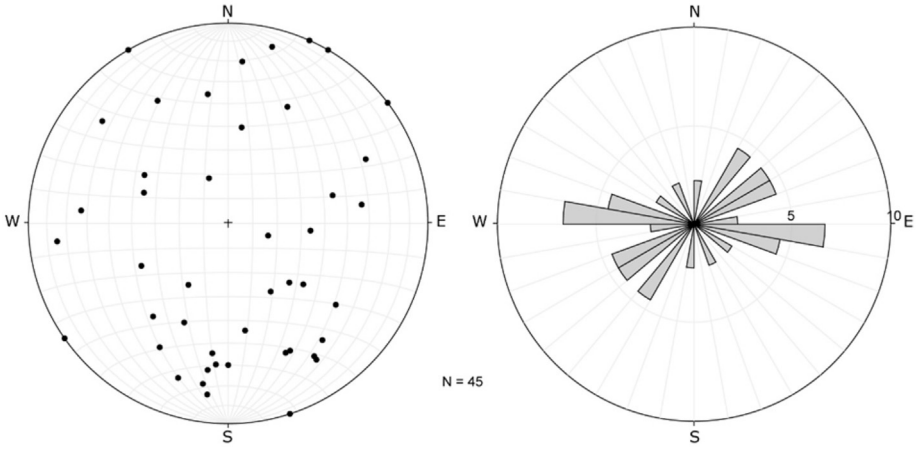

Fig. 7. Lower hemisphere, equal-area projection shows wide orientation range for veins throughout Tol-1 core: (a) poles veins (b) petals each 10°.

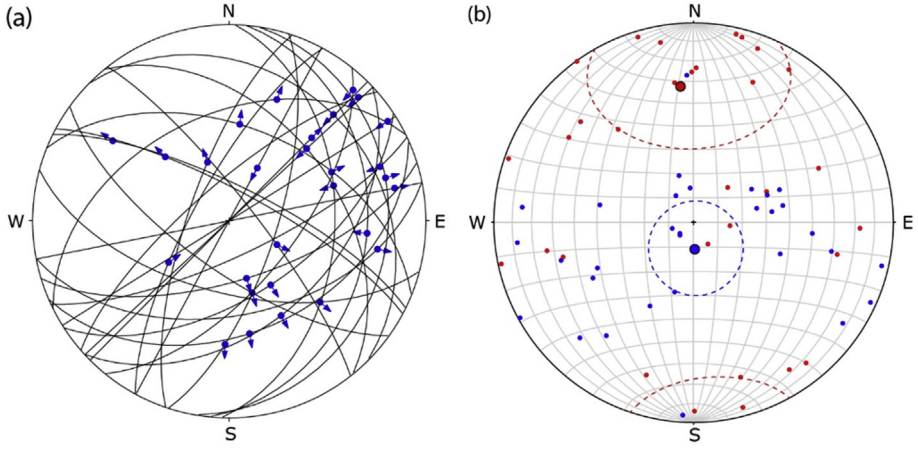

Fig. 8. (a) Fault-slip data mapped on the borehole Tol-1. (b) Lower hemisphere, equal-area projection showing the calculated strain axes (using Faultkin 7.4). P- and T-axes of each fault (blue and red dot, respectively) with their mean vectors (blue and red circle) and error ellipse (dashed line). (For interpretation of the references to colour in this figure legend, the reader is referred to the web version of this article.)

prehnite, quartz, pyrite, and less common chalcedony and chlorite/smectite dominate the deep zone (>700 m); indicating a propylitic alteration type. Similar to the veins and hybrid faults observed up-hole, here, these structural elements are predominantly NNE-ENE-striking and >50° dipping. Veins show a preferential striking EW to ENE (Fig. 7), with thicknesses that vary throughout the core between 1 and 20 mm.

4.3. Strain field

Fault-slip data inversion (Fig. 8a) yielded a widely-scattered distribution for both P- and T-axes clusters (Fig. 8b). P-axes are roughly distributed along a major girdle on an EW direction whereas T-axes are scattered about N and S orientations (Fig. 8b). The mean shortening vector is oriented 352°/38° (95 per cent confidence cone, $\alpha_{95} > 20°$) and the stretching vector is 177°/78° ($\alpha_{95} = 19°$).

4.4. Stress field

Dynamic analysis shows a well-defined orientation for both clusters of σ_1 and σ_3 axes (Fig. 9a), with a normal-like distribution of φ values (maximum value $\varphi = 0.4$) (Fig. 9c). This analysis indicates a tensional tectonic regime with vertical σ_1 (083°/74°) and N-trending subhorizontal σ_3 (184°/03°) (Fig. 9b). The angular misfit (Fig. 9d) indicates that nearly all the analyzed faults respond to a common stress field.

5. Discussion

5.1. Magnetic reorientation

Deformation genetically associated with LOFS and ATF mostly records *in situ* tectonic blocks rotations (Cembrano et al., 1992; Hernandez-Moreno et al., 2016, 2014). Paleomagnetic evidence (Hernandez-Moreno et al., 2016, 2014) report that tectonic blocks next to the LOFS (measured on Mio-Pliocene rocks) record mainly N-ward translation without a significant rotation. However, sub-circular blocks undergo great rotation. We assumed that the tectonic block containing the Tol-1 core has no significant rotation. Hence, we use the GAD reference frame to restore the different pieces and structural elements. GAD has associated a paleo-secular variation error of ±20°, which is considered in the stress field orientation result.

Thermal step-wise demagnetization suggests that magnetite and hematite mineral phases are the main carriers of the remanent

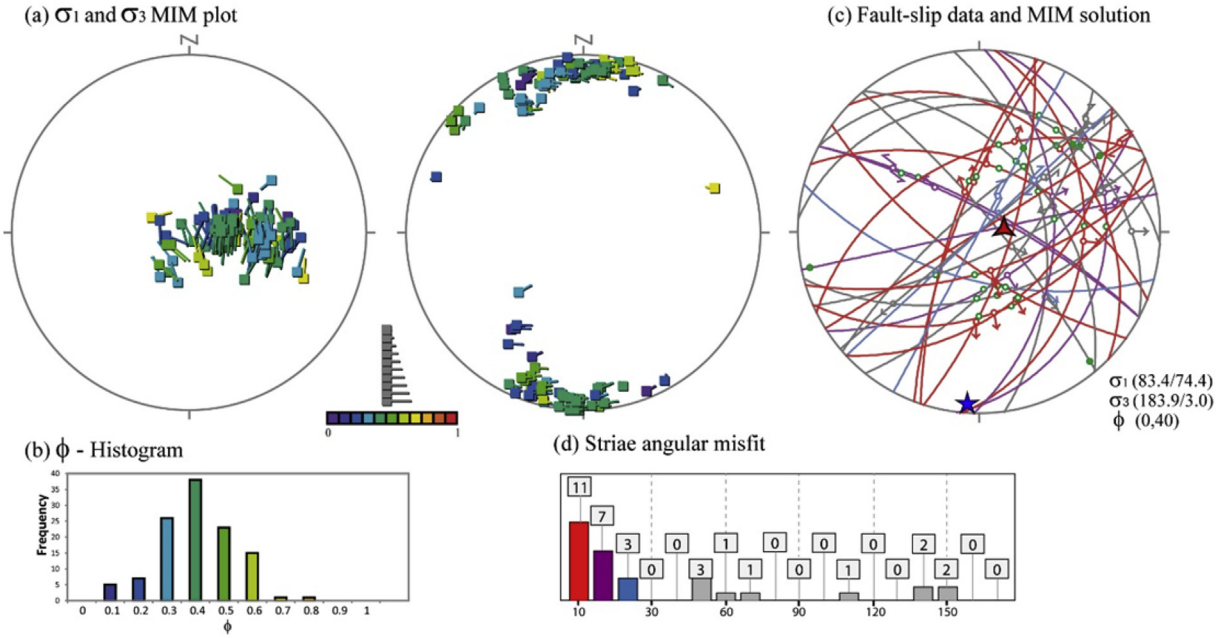

Fig. 9. (a) Stress field solutions as given by the MIM applied to the fault-slip data. Results show σ_1 (rightwards) and σ_3 (leftwards) axes plotted on a lower hemisphere equal-area projection; the color represents the φ-value from purple - red (0–1, respectively). (b) φ-histogram graphic shows a unimodal distribution with maximum value at $\varphi = 0.4$. (c) Lower hemisphere, equal-area projection shows stress field best solution, vertical σ_1-axis (83/74) (red triangle) and horizontal σ_3-axis (184/3) (blue star); fault-slip data colors represent the misfit value. (d) Misfit value histogram between real and modeled striae calculated by MIM. (For interpretation of the references to colour in this figure legend, the reader is referred to the web version of this article.)

magnetic signal (Fig. 6c). We recognized blocking temperatures in the range of (400°–600 °C) which most probably depict a variable titanium content in magnetite from TM60 to TM100 (Dunlop and Ozdemir, 2000; Winklhofer et al., 1997) (Fig. 6c). Well-defined ChRMs in mostly all piece of the Tol-1 core allowed to re-orient most veins and faults. Inclinations of ChRM vectors downcore (Fig. 6d) record normal polarity.

Although there are no available absolute ages for the whole Tol-1 rock sequence, the oldest rock units of Tolhuaca and Lonquimay volcanoes are 290 ky old (Ar-Ar whole rock method, Polanco et al., 2014) and 700–400 ky (Moreno et al., 2012) respectively. This is consistent with one of the oldest volcanic units dated in the southern volcanic zone corresponding to 600 ± 70 Ka, at the base of Villarrica volcano, (Ar-Ar whole rock method, Moreno and Clavero, 2006). These stratigraphic ages constraints combined with the magnetic normal polarity documented in this work along the Tol-1 core, suggest that the natural magnetization identified in the Tol-1 core rock sequence was acquired at some time during Brunhes polarity chron (0–780 ka) (Suganuma et al., 2015).

Re-orienting the original structures hosted by sedimentary rocks implies making more critical assumptions than for volcanic rocks because sedimentary rocks do not necessarily hold their primary magnetization (Parés et al., 2008; Zhang et al., 2007). Nevertheless, volcanic rocks can undergo magnetic overprinting. The Tolhuaca volcanic sequence has excellent lithological and magnetic conditions for paleomagnetic core-reorientation, especially because they are young volcanic rocks not affected by Mio-Pleistocene locally tectonic rotations (Hernandez-Moreno et al., 2016, 2014). The hydrothermal alteration recognized along the core is characteristic of a temperature lower than 350 °C while the blocking temperature of magnetic mineralogy is between 400° and 600 °C. These temperature difference and the single demagnetization patterns support that the titano-magnetite minerals carry the primary magnetization.

5.2. Re-oriented structural elements and the regional tectonic setting

At regional scale the northern termination of Liquiñe-Ofqui Fault System records a transpressional tectonic regime with a N65E-trending σ_1 axis and a N30W-trendig σ_3 axis (Fig. 10) (e.g. Cembrano et al., 2000; Lavenu and Cembrano, 1999; Pérez-Flores et al., 2016). This regional tectonic regime results from the local stress/strain field variations within the fault zone which depends,

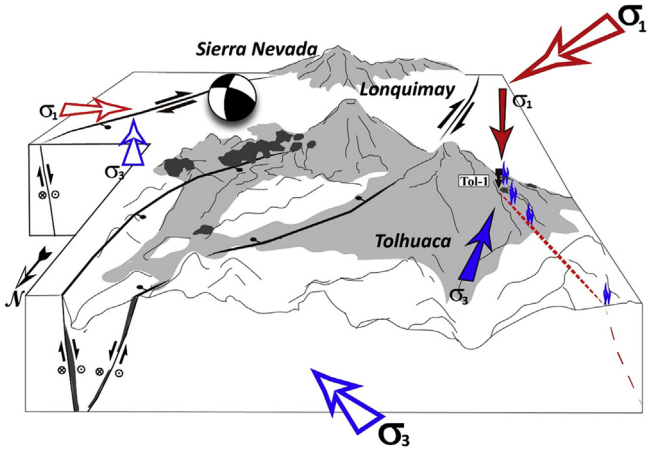

Fig. 10. Schematic block diagram illustrating the proposed tectonic setting of Tolhuaca-Lonquimay volcanoes (looking south). The model shows the spatial distribution of flank-vents (dark grey), fumaroles (blue flames), stratovolcanoes and faults, which are kinematically compatible with regional stress field (biggest unfilled arrows) (Lavenu and Cembrano, 1999; Pérez-Flores et al., 2016), previous calculated local stress field (unfilled arrows) (Pérez-Flores et al., 2016) and our stress field solution (filled arrows) at the Tol-1 core location. (For interpretation of the references to colour in this figure legend, the reader is referred to the web version of this article.)

among other things, on specific fault orientations (Pérez-Flores et al., 2016). In this context, our fault-slip data record a strain field where the orientation of both P- and T-axes shows a wide-ranging distribution. Multi-modal patterns of P- and T-axes reveal a kinematically heterogeneous faulting, which is probably produced by anisotropy reactivation and/or multiple deformation (Marrett and Allmendinger, 1990). The local deformation can reactivate pre-existing anisotropies that are not ideally oriented for accommodating deformation. This reactivation can be promoted by high fluid pressure in the geothermal system (Barnhoorn et al., 2010; Cox, 2010; Sibson, 2012, 1985). High fluid pressure is likely to have occurred in the TGS, as indicated by numerical simulations and the mineralogical observations (Sanchez-Alfaro et al., 2016).

On the contrary, calculated stress fields yielded clear σ_1-and σ_3-axes clusters that indicate a local tensional tectonic regime with vertical compression (σ_1) and NS-tension (σ_3), which is compatible with a transtensional regional stress field solution independently documented from field work in the area (Pérez-Flores et al., 2016). Southeast of Lonquimay volcano, Pérez-Flores et al. (2016), identified similar minimum stress axis orientation (σ_3) under a bulk transpressional local stress field within a NE-striking fault (Fig. 10). At both locations, local stress field orientations are kinematically compatible with ENE-to EW-striking tensional fractures. Focal mechanisms of shallow (<25 km) earthquakes located within the NE-striking releasing bend (LOFS) at Lonquimay volcano (Fig. 10) (Barrientos and Acevedo-Aránguiz, 1992; Dziewonski et al., 1990) and the NE-striking fault below the Callaqui volcano (http://www.globalcmt.org/CMTsearch.html) (Fig. 1b) are consistent with NS maximum extension and EW shortening. Focal mechanisms, ENE-trending flank-vents alignment and the Lonquimay ENE-striking volcanic fissure (Pérez-Flores et al., 2016; Rosenau et al., 2006) are consistent with the NS maximum extension recorded at the Tolhuaca volcano (Fig. 10). Similarly, focal mechanisms of the Aysén seismic swarm (2007) located at the southern termination of LOFS identified NE-striking normal and NS-striking right-lateral strike-slip faults coeval with magma/fluid activity (e.g. ; Legrand et al., 2011; Russo et al., 2011), which support our tensional stress field result and the extensional deformation at the NE- and ENE-striking faults spatially associated with NS-striking faults (LOFS).

Under this local stress field, both NE- and NW-striking discontinuities can be activated, developing complex fault-vein networks and promoting magma/fluid ascent, conducive to synchronous volcanic activity within NE-striking and NW-striking fissure at Lonquimay and Tolhuaca volcanoes, respectively.

Vein networks display two slightly distinctive orientations: EW- and NE-striking. The EW-striking veins are kinematically compatible with the calculated local stress field and with the third-order structures described at regional scale (Pérez-Flores et al., 2016). The NE-striking veins are kinematically compatible with the regional stress field, volcanoes elongation, alignment of flank-vents and dikes orientation (e.g. Bouvet de Maisonneuve et al., 2012; Pérez-Flores et al., 2016; Sielfeld et al., 2016).

Strike and dip distribution of faults and veins throughout the Tol-1 core (Fig. 6d and e) shows that within the upper argillic alteration zone (<400 m), these are randomly oriented with variable dipping angles (20°–90°). Below the clay-cap (sub-propylitic zone, > 300 m), we identified a weakly-defined NNE-ENE-striking arrangement of veins and faults, down to the borehole bottom. The deeper zone (>700 m) mostly records steeply-dipping > 50° veins and faults. These results suggest that the control of the local and regional stress field on veins and faults orientation strongly faints at shallow depth, with reduced vertical stress (σ_1) and lithostatic pressure. Although a tensional tectonic regime promotes steeply-dipping vein-networks (e.g. Faulkner and Armitage, 2013; Sibson, 1996), our results show that the vertical faults and veins best observed below 700 m deep (Fig. 6e).

6. Conclusions

i. This work is the first successful attempt to reorient a core with paleomagnetic methodology in the Chilean southern volcanic zone and proved to be an efficient and cost-effective technique for re-orient veins and fault to geographical coordinates throughout non-oriented drill cores.
ii. The heterogeneous deformation documented by strain analysis of the fault population probably occurred by anisotropy reactivation of pre-existing discontinuities promoted by high fluid pressure within the geothermal system, under a tensional local stress field with NS-trending tension and EW-compression axes.
iii. The prevailing transpressional regional stress field within the intra-arc zone, with NE-trending σ_1 and NW-trending σ_3, is locally accommodated at the NE-striking fault zones with clearly defined N- to NNW-trending tension and E-to ENE-trending compression axes. The tensional local stress field at the Tolhuaca area can be explained as a switch between σ_1 and σ_2 main stress axes as driven by local extension at the Lonquimay releasing bend structure within the LOFS and/or locally low lithospheric pressure at the Tol-1 core depth (1020 m).
iv. The vertically oriented σ_1 and horizontally N-trending σ_3 axes are kinematically compatible with ENE- and WNW-striking hybrid faults and EW-striking extensional veins. This tectonic environment can promote a synchronous volcanism or hydrothermal activity along either NE and/or NW volcanic vent fissures.
v. The N-trending σ_3 axis is compatible with earthquake focal mechanisms available for the area showing consistency of the long- and short-term intra-arc tectonics.
vi. Our results attest that the tensional local stress field at the Tolhuaca Geothermal System has weak control on the spatial distribution of veins orientations above 700 m depth which increase below 700 m.

Acknowledgements

CONICYT-FONDAP Project Andean Geothermal Centre of Excellence 15090013 (CEGA) is funding this research. Perez-Flores's PhD studies are funded by CONICYT — Beca Doctorado Nacional 21120519 and Sanchez-Alfaro acknowledges support given by Millennium Science Initiative grant NC130065. We thank MRP-Chile Ltd. and former GGE Ltd., S. Iriarte, S. Lohmar, G. Melosh, J. Stimac and A. Colvin for providing access to Tolhuaca and for the information and samples used in this study. We sincerely thank Associated Editor Ian Alsop and reviewers Fabio Speranza and Anita Di Chiara, they provided very useful comments and criticism that helped to improve the manuscript. Thanks to Herrera, E. for laboratory runs and Rubilar, J. for his help in the field work. Thanks to P. Iturrieta. for his important help with the data analysis and R. Gomila. for his helpful revision of the manuscript.

Appendix A. Supplementary data

Supplementary data related to this article can be found at http://dx.doi.org/10.1016/j.jsg.2017.01.009.

References

Alstine, D.R., Van Butterworth, J.E., 2002. Paleomagnetic core-orientation helps determine the sedimentological, paleostress, and fluid-migration history in the

Maracaibo basin, Venezuela. In: Core Workshop for I Congreso de Sedimentología. Applied Paleomagnetics, Inc, pp. 1–29.
Barnhoorn, A., Cox, S.F., Robinson, D.J., Senden, T., 2010. Stress- and fluid-driven failure during fracture array growth: implications for coupled deformation and fluid flow in the crust. Geology 38, 779–782. http://dx.doi.org/10.1130/G31010.1.
Barrientos, S.E., Acevedo-Aránguiz, P.S., 1992. Seismological aspects of the 1988–1989 Lonquimay (Chile) volcanic eruption. J. Volcanol. Geotherm. Res. 53, 73–87. http://dx.doi.org/10.1016/0377-0273(92)90075-O.
Bons, P.D., Elburg, M.A., Gomez-Rivas, E., 2012. A review of the formation of tectonic veins and their microstructures. J. Struct. Geol. 43, 33–62. http://dx.doi.org/10.1016/j.jsg.2012.07.005.
Bouvet de Maisonneuve, C., Dungan, M.A., Bachmann, O., Burgisser, A., 2012. Insights into shallow magma storage and crystallization at Volcán Llaima (andean southern volcanic zone, Chile). J. Volcanol. Geotherm. Res. 211–212, 76–91. http://dx.doi.org/10.1016/j.jvolgeores.2011.09.010.
Brogi, A., 2008. Fault zone architecture and permeability features in siliceous sedimentary rocks: insights from the Rapolano geothermal area (Northern Apennines, Italy). J. Struct. Geol. 30, 237–256. http://dx.doi.org/10.1016/j.jsg.2007.10.004.
Butler, R.F., 1998. PALEOMAGNETISM. Magnetic Domains to Geologic Terranes, University, Tucson, Arizona.
Cembrano, J., Garcia, A., Herve, F., 1992. Paleomagnetism of Lower Cretaceous rocks from east of the Liquine-Ofqui fault zone, southern Chile: evidence of small in-situ clockwise rotations. Earth Planet. Sci. Lett. 113, 539–551. http://dx.doi.org/10.1016/0012-821X(92)90130-N.
Cembrano, J., Lara, L., 2009. The link between volcanism and tectonics in the southern volcanic zone of the Chilean Andes: a review. Tectonophysics 471, 96–113. http://dx.doi.org/10.1016/j.tecto.2009.02.038.
Cembrano, J., Schermer, E., Lavenu, A., Sanhueza, A., 2000. Contrasting nature of deformation along an intra-arc shear zone, the Liquiñe – Ofqui fault zone, southern Chilean Andes. Tectonophysics 319, 129–149. http://dx.doi.org/10.1016/S0040-1951(99)00321-2.
Cox, S.F., 2010. The application of failure mode diagrams for exploring the roles of fluid pressure and stress states in controlling styles of fracture-controlled permeability enhancement in faults and shear zones. Geofluids 217–233. http://dx.doi.org/10.1111/j.1468-8123.2010.00281.x.
Curewitz, D., Karson, J.A., 1997. Structural settings of hydrothermal outflow: fracture permeability maintained by fault propagation and interaction. J. Volcanol. Geotherm. Res. 79, 149–168. http://dx.doi.org/10.1016/S0377-0273(97)00027-9.
Didenko, A.N., 1996. Modification of the borehole core orientation method with the use of viscous magnetization. Phys. Solid Earth 31, 879–884.
Doblas, M., 1998. Slickenside kinematic indicators. Tectonophysics 295, 187–197. http://dx.doi.org/10.1016/S0040-1951(98)00120-6.
Dobson, P.F., Kneafsey, T.J., Hulen, J., Simmons, A., 2003. Porosity, permeability, and fluid flow in the Yellowstone geothermal system. Wyo. J. Volcanol. Geotherm. Res. 123, 313–324. http://dx.doi.org/10.1016/S0377-0273(03)00039-8.
Dunlop, D.J., Ozdemir, O., 2000. Effect of grain size and domain state on thermal demagnetization tails. Geophys. Res. Lett. 27, 1311–1314. http://dx.doi.org/10.1029/1999GL008461.
Dziewonski, A.M., Ekström, G., Woodhouse, J.H., Zwart, G., 1990. Centroid-moment Tensor Solutions for January–. March 1989, vol. 59, pp. 233–242.
Faulkner, D.R., Armitage, P.J., 2013. The effect of tectonic environment on permeability development around faults and in the brittle crust. Earth Planet. Sci. Lett. 375, 71–77. http://dx.doi.org/10.1016/j.epsl.2013.05.006.
Ganerød, G.V., Braathen, A., Willemoes-Wissing, B., 2008. Predictive permeability model of extensional faults in crystalline and metamorphic rocks; verification by pre-grouting in two sub-sea tunnels. Nor. J. Struct. Geol. 30, 993–1004. http://dx.doi.org/10.1016/j.jsg.2008.04.001.
Glodny, J., Gräfe, K., Echtler, H., Rosenau, M., 2007. Mesozoic to Quaternary continental margin dynamics in South-Central Chile (36–42°S): the apatite and zircon fission track perspective. Int. J. Earth Sci. 97, 1271–1291. http://dx.doi.org/10.1007/s00531-007-0203-1.
Hailwood, E.A., Ding, F., 1995. Palaeomagnetic re-orientation of cores and the magnetic fabric of hydrocarbon reservoir sands. Palaeomagnetic Appl. Hydrocarb. Explor. Prod. 98, 245–258. http://dx.doi.org/10.1144/GSL.SP.1995.098.01.15.
Hauser, A., 1997. Catastro y caracterizacion de las fuentes de aguas minerales y termales de Chile. SERNAGEOMIN, Santiago, p. 77.
Hernandez-Moreno, C., Speranza, F., Di Chiara, A., 2016. Paleomagnetic rotation pattern of the southern Chile fore-arc sliver (38°S–42°S): a new tool to evaluate plate locking along subduction zones. J. Geophys. Res. Solid Earth 121, 469–490. http://dx.doi.org/10.1002/2015JB012382.
Hernandez-Moreno, C., Speranza, F., Di Chiara, A., 2014. Understanding kinematics of intra-arc transcurrent deformation: paleomagnetic evidence from the Liquiñe-Ofqui fault zone (Chile, 38-41°S). Tectonics 33, 1964–1988. http://dx.doi.org/10.1002/2014TC003622.
Hulton, N.R.J., Purves, R.S., McCulloch, R.D., Sugden, D.E., Bentley, M.J., 2002. The last glacial maximum and deglaciation in southern south America. Quat. Sci. Rev. 21, 233–241. http://dx.doi.org/10.1016/S0277-3791(01)00103-2.
Kaplan, M.R., Moreno, P.I., Rojas, M., 2008. Glacial dynamics in southernmost South America during Marine Isotope Stage 5e to the Younger Dryas chron: a brief review with a focus on cosmogenic nuclide measurements. J. Quat. Sci. 23 (6–7), 649–658. http://dx.doi.org/10.1002/jqs.1209.
Kirschvink, J.L., 1980. The least-squares line and plane and the analysis of paleomagnetic data. Geophys. J. R. Astron. Soc. 62, 699–718. http://dx.doi.org/10.1111/j.1365-246X.1980.tb02601.x.
Lange, D., Cembrano, J., Rietbrock, A., Haberland, C., Dahm, T., Bataille, K., 2008. First seismic record for intra-arc strike-slip tectonics along the Liquiñe-Ofqui fault zone at the obliquely convergent plate margin of the southern Andes. Tectonophysics 455, 14–24. http://dx.doi.org/10.1016/j.tecto.2008.04.014.
Lara, L., Lavenu, A., Cembrano, J., Rodriguez, C., 2006. Structural controls of volcanism in transversal chains: resheared faults and neotectonics in the Cordón Caulle–Puyehue area (40.5°S), Southern Andes. J. Volcanol. Geotherm. Res. 158, 70–86. http://dx.doi.org/10.1016/j.jvolgeores.2006.04.017.
Lavenu, A., Cembrano, J., 1999. Compressional- and transpressional-stress pattern for Pliocene and Quaternary brittle deformation in fore arc and intra-arc zones (Andes of Central and Southern Chile). J. Struct. Geol. 21, 1669–1691. http://dx.doi.org/10.1016/S0191-8141(99)00111-X.
Legrand, D., Barrientos, S., Bataille, K., Cembrano, J., Pavez, A., 2011. The fluid-driven tectonic swarm of Aysen Fjord, Chile (2007) associated with two earthquakes (Mw=6.1 and Mw=6.2) within the Liquiñe-Ofqui Fault Zone. Cont. Shelf Res. 31, 154–161. http://dx.doi.org/10.1016/j.csr.2010.05.008.
Lizama, M., Reich, M., Sánchez-Alfaro, P., Pérez-Flores, P., Cembrano, J., Morata, D., Arancibia, G., 2015. In: Alteración hidrotermal en el pozo Tol-1, Sistema Geotermal Tolhuaca, Chile: un nuevo modelo de capa sello en sistemas geotermales andinos, in: XIV Congreso Geológico Chileno. La Serena, pp. 473–476.
Lohmar, S., Stimac, J., Colvin, A., González, A., Iriarte, S., Melosh, G., Wilmarth, M., 2012. Tolhuaca volcano (Southern Chile, 38.3°S): new learnings from surface mapping and geothermal exploration wells. In: Proc. Congr. Geológico Chil. 2012 Antofagasta, Chile, 5-9 August 2012, pp. 443–445.
MacLeod, C.J., Parson, L.M., Sager, W., 1994. Reorientation of cores using the formation microscanner and borehole televiewer: application to structural and paleomagnetic studies with the ocean drilling program. Proc. Ocean. Drill. Progr 135, 301–311. http://dx.doi.org/10.2973/odp.proc.sr.135.160.1994.
Marrett, R., Allmendinger, R.W., 1990. Kinematic analysis of fault-slip data. J. Struct. Geol. 12, 973–986. http://dx.doi.org/10.1016/0191-8141(90)90093-E.
McCulloch, R.D., Bentley, M.J., Purves, R.S., Hulton, N.R.J., Sugden, D.E., Clapperton, C.M., 2000. Climatic inferences from glacial and palaeoecological evidence at the last glacial termination, southern South America. J. Quat. Sci. 15, 409–417. http://dx.doi.org/10.1002/1099-1417(200005)15, 4<409::AID-JQS539>3.0.CO;2-#.
Melnick, D., Folguera, A., Ramos, V., 2006. Structural control on arc volcanism: the caviahue–copahue complex, central to patagonian Andes transition (38°S). J. South Am. Earth Sci. 22, 66–88. http://dx.doi.org/10.1016/j.jsames.2006.08.008.
Melosh, G., Cumming, W., Benoit, D., Wilmarth, M., Colvin, A., Winick, J., Soto, E., Sussman, D., Urzúa-monsalve, L., Powell, T., Peretz, A., 2010. Exploration results and resource conceptual model of the Tolhuaca Gethermal Field, Chile. In: Proceedings World Geothermal Congress. Bali, Indonesia, pp. 25–29.
Melosh, G., Moore, J., Stacey, R., 2012. Natural reservoir evolution in the Tolhuaca geothermal field, southern Chile. In: Thirty-sixth Workshop on Geothermal Reservoir Engineering. Stanford, California, United States.
Moncada, D., Mutchler, S., Nieto, A., Reynolds, T.J., Rimstidt, J.D., Bodnar, R.J., 2012. Mineral textures and fluid inclusion petrography of the epithermal Ag–Au deposits at Guanajuato, Mexico: application to exploration. J. Geochem. Explor 114, 20–35. http://dx.doi.org/10.1016/j.gexplo.2011.12.001.
Moreno, H., Clavero, J., 2006. Geología del Volcán Villarrica. Carta geológica de Chile 1:50.000. SERNAGEOMIN, Chile.
Moreno, H., Naranjo, J., Polanco, E., 2012. Geología del complejo volcánico Lonquimay-Tolhuaca. Carta Geológica de Chile 1:50.000. SERNAGEOMIN, Chile.
Muñoz, J., Stern, C.R.R., Muñoz, B.J., Stern, C.R.R., 1988. The quaternary volcanic belt of the southern continental margin of South America: transverse structural and petrochemical variations across the segment between 38°S and 39°S. J. South Am. Earth Sci. 1, 147–161. http://dx.doi.org/10.1016/0895-9811(88)90032-6.
Nakamura, K., 1977. Volcanoes as possible indicators of tectonic stress orientation - principle and proposal. J. Volcanol. Geotherm. Res. 2, 1–16. http://dx.doi.org/10.1007/BF01637099.
Nukman, M., Moeck, I., 2013. Structural controls on a geothermal system in the Tarutung Basin, north central Sumatra. J. Asian Earth Sci. 74, 86–96. http://dx.doi.org/10.1016/j.jseaes.2013.06.012.
Otsubo, M., Sato, K., Yamaji, A., 2006. Computerized identification of stress tensors determined from heterogeneous fault-slip data by combining the multiple inverse method and k-means clustering. J. Struct. Geol. 28, 991–997. http://dx.doi.org/10.1016/j.jsg.2006.03.008.
Parés, J.M., Schleicher, A.M., van der Pluijm, B.A., Hickman, S., 2008. Paleomagnetic reorientation of san Andreas fault observatory at depth (SAFOD) core. Geophys. Res. Lett. 35, 1–6. http://dx.doi.org/10.1029/2007GL030921.
Pérez-Flores, P., Cembrano, J., Sanchez, P., Veloso, E., Arancibia, G., Roquer, T., 2016. Tectonics, magmatism and paleo-fluid distribution in a strike-slip setting: insights from the northern termination of the Liquiñe-Ofqui fault System, Chile. Tectonophysics 680, 192–210. http://dx.doi.org/10.1016/j.tecto.2016.05.016.
Petit, J.P., 1987. Criteria for the sense o f movement on fault surfaces in brittle rocks. J. Struct. Geol. 9, 597–608. http://dx.doi.org/10.1016/0191-8141(87)90145-3.
Polanco, E., Moreno, H., Naranjo, J.A., Pérez de Arce, C., 2014. Nuevas edades Ar/Ar del Complejo Lonquimay-Tolhuaca y su contribución a la comprensión de su evolución geológica. In: Jornadas Geológicas, Sesión Temática 12. SERNAGEOMIN, Santiago, Chile, pp. 139–142.
Radic, J.P., 2010. Las cuencas cenozoicas y su control en el volcanismo de los

Complejos Nevados de Chillán y Copahue-Callaqui (Andes del Sur, 36-39 ° S). Andean Geol. 37, 220–246.
Reyes, A.G., 1990. Petrology of Philippine geothermal systems and the application of alteration mineralogy to their assessment. J. Volcanol. Geotherm. Res. 43, 279–309. http://dx.doi.org/10.1016/0377-0273(90)90057-M.
Ritz, J.-F., 1994. Determining the slip vector by graphical construction: use of a simplified representation of the stress tensor. J. Struct. Geol. 16, 737–741.
Rosenau, M., Melnick, D., Echtler, H., 2006. Kinematic constraints on intra-arc shear and strain partitioning in the southern Andes between 38 ° S and 42 ° S latitude. Tectonics 25, 1–16. http://dx.doi.org/10.1029/2005TC001943.
Rowland, J.V., Sibson, R.H., 2004. Structural controls on hydrothermal flow in a segmented rift system, Taupo Volcanic Zone, New Zealand. Geofluids 4, 259–283. http://dx.doi.org/10.1111/j.1468-8123.2004.00091.x.
Rowland, J.V., Simmons, S.F., Zealand, N., Zealand, N., 2012. Hydrologic, magmatic, and tectonic controls on hydrothermal flow, taupo volcanic zone, New Zealand: implications for the formation of epithermal vein deposits. Econ. Geol. 107, 427–457. http://dx.doi.org/10.2113/econgeo.107.3.427.
Russo, R., Mora-stock, C., Vandecar, J.C., Russo, R.M., Gallego, A., Comte, D., Mocanu, V.I., Murdie, R.E., Mora, C., Vandecar, J.C., 2011. Triggered seismic activity in the Liquiñe-Ofqui fault zone, southern Chile, during the 2007 Aysen seismic swarm Chile, during the 2007 Aysen seismic swarm. Geophys. J. Int. 184, 1217–1326. http://dx.doi.org/10.1111/j.1365-246X.2010.04908.x.
Sánchez, P., Pérez-Flores, P., Reich, M., Arancibia, G., Cembrano, J., 2013. Crustal deformation effects on the chemical evolution of geothermal systems: the intra-arc Liquiñe–Ofqui Fault System, Southern Andes. Int. Geol. Rev. 55, 37–41. http://dx.doi.org/10.1080/00206814.2013.775731.
Sanchez-Alfaro, P., Reich, M., Arancibia, G., Pérez-Flores, P., Cembrano, J., Driesner, T., Lizama, M., Rowland, J., Morata, D., Heinrich, C.C.A., Tardani, D., Campos, E., 2016. Physical, chemical and mineralogical evolution of the Tolhuaca geothermal system, southern Andes, Chile: insights into the interplay between hydrothermal alteration and brittle deformation. J. Volcanol. Geotherm. Res. 324, 88–104. http://dx.doi.org/10.1016/j.jvolgeores.2016.05.009.
Sepúlveda, F., Lahsen, A., Bonvalot, S., Cembrano, J., Alvarado, A., Letelier, P., 2005. Morpho-structural evolution of the cordón caulle geothermal region, southern volcanic zone, Chile: insights from gravity. J. Volcanol. Geotherm. Res. 148, 165–189. http://dx.doi.org/10.1016/j.jvolgeores.2005.03.020.
Sibson, R.H., 2012. Reverse fault rupturing;: competition between non-optimal and optimal fault orientations Reverse fault rupturing: competition between non-optimal and optimal fault orientations. Geol. Soc. Lond. Spec. Publ. 367, 39–50. http://dx.doi.org/10.1144/SP367.4.
Sibson, R.H., 1996. Structural permeability of fluid-driven fault-fracture meshes. J. Struct. Geol. 18, 1031–1042. http://dx.doi.org/10.1016/0191-8141(96)00032-6.
Sibson, R.H., 1985. A note on fault reactivation. J. Struct. Geol. 7, 751–754.
Sielfeld, G., Cembrano, J., Lara, L., 2016. Transtension driving volcano-edifice anatomy: insights from Andean transverse-to-the-orogen tectonic domains. Quat. Int. 1–17 http://dx.doi.org/10.1016/j.quaint.2016.01.002.
Stimac, J., Goff, F., Goff, C.J., 2015. Intrusion-related geothermal systems. In: The Encyclopedia of Volcanoes, second ed. http://dx.doi.org/10.1016/B978-0-12-385938-9.00046-8 Dr Jim Stimac, Copyright © 2015.
Suárez, M., Emparan, C., 1997. Hoja Curacautín, región de la Araucanía y del Biobío. Carta geológica de Chile. In: Servicio, N. (Ed.), Carta Geológica de Chile, Servicio Nacional de Geología y Minería.
Suganuma, Y., Okada, M., Horie, K., Kaiden, H., Takehara, M., Senda, R., Kimura, J.I., Kawamura, K., Haneda, Y., Kazaoka, O., Head, M.J., 2015. Age of Matuyama-Brunhes boundary constrained by U-Pb zircon dating of a widespread tephra. Geology 43, 491–494. http://dx.doi.org/10.1130/G36625.1.
Tardani, D., Reich, M., Roulleau, E., Takahata, N., Sano, Y., Pérez-Flores, P., Sánchez, P., Cembrano, J., Arancibia, G., Sánchez-Alfaro, P., Cembrano, J., Arancibia, G., Sa, P., Sano, Y., Pe, P., Arancibia, G., 2016. Exploring the structural controls on helium, nitrogen and carbon isotope signatures in hydrothermal fluids along an intra-arc fault system. Geochim. Cosmochim. Acta 184, 193–211. http://dx.doi.org/10.1016/j.gca.2016.04.031.
Tauxe, L., 1998. Paleomagnetic Principles and Practice. In: Mod. Approach. Geophys.. Kluwer Academic Publishers, Dordrecht; Boston xi, 299p.
Thiele, R., Lahsen, A., Moreno, H., Varela, J., Vergara, M., 1987. Estudios geológicos regionales a escala 1:100.000 de la hoya superior y curso medio del Biobío.
Ureel, S., Momayez, M., Oberling, Z., 2013. Rock core orientation for mapping discontinuities and. Int. J. Res. Eng. Technol. 02, 1–8.
Veloso, E.E., Anma, R., Yamaji, A., 2009. Ophiolite emplacement and the effects of the subduction of the active Chile ridge system: heterogeneous paleostress regimes recorded in the taitao Ophiolite (southern Chile). Andean Geol. 36, 3–16. http://dx.doi.org/10.5027/andgeoV36n1-a01.
Virgil, C., Ehmann, S., Hordt, A., Leven, M., Steveling, E., 2015. Reorientation of three-component borehole magnetic data. Geophys. Prospect 63, 225–242. http://dx.doi.org/10.1111/1365-2478.12175.
Winklhofer, M., Fabian, K., Heider, F., 1997. Magnetic blocking temperatures of magnetite calculated with a three-dimensional micromagnetic model. J. Geophys. Res. 102, 22695–22709. http://dx.doi.org/10.1029/97JB01730.
Whitney, D.L., Evans, B.W., 2010. Abbreviations for names of rock-forming minerals. Am. Miner. 95, 185–187. http://dx.doi.org/10.2138/am.2010.3371.
Yamaji, A., 2000. The multiple inverse method: a new technique to separate stresses from heterogeneous fault-slip data. J. Struct. Geol. 22, 441–452. http://dx.doi.org/10.1016/S0191-8141(99)00163-7.
Zhang, F.-Q., Song, J.-S., Shen, Z.-Y., Chen, H.-L., Dong, C.-W., Pang, Y.-M., Shu, P., 2007. A study on fracture orientation and characteristic of remnant magnetization of deep-burial volcanic rocks, north of the Songliao Basin. Chin. J. Geophys. 50, 1011–1017. http://dx.doi.org/10.1002/cjg2.1118.
Zhang, Y., Schaubs, P.M., Zhao, C., Ord, A., Hobbs, B.E., Barnicoat, A.C., 2008. Fault-related dilation, permeability enhancement, fluid flow and mineral precipitation patterns: numerical models. Geol. Soc. Lond. Spec. Publ. 299, 239–255. http://dx.doi.org/10.1144/SP299.15.
Zijderveld, J.D.A., 1967. A.C. Demagnetization of rocks: analysis of results. In: Collinson, D.W., Creer, K.M., Runcorn, S.K. (Eds.), Methods in Paleomagnetism. Elsevier, Amsterdam.